



# Partitioning of $\text{Fe}_2\text{O}_3$ in peridotite partial melting experiments over a range of oxygen fugacities elucidates ferric iron systematics in mid-ocean ridge basalts and ferric iron content of the upper mantle

Fred A. Davis<sup>1,2</sup> · Elizabeth Cottrell<sup>2</sup>

Received: 13 April 2021 / Accepted: 26 July 2021 / Published online: 12 August 2021

This is a U.S. government work and not under copyright protection in the U.S.; foreign copyright protection may apply 2021

## Abstract

Basalts and peridotites from mid-ocean ridges record  $f_{\text{O}_2}$  near the quartz-fayalite-magnetite buffer (QFM), but peridotite partial melting experiments have mostly been performed in graphite capsules (~QFM-3), precluding evaluation of ferric iron's behavior during basalt generation. We performed experiments at 1.5 GPa, 1350–1400 °C, and  $f_{\text{O}_2}$  from about QFM-3 to QFM+3 to investigate the anhydrous partitioning behavior of  $\text{Fe}_2\text{O}_3$  between silicate melts and coexisting peridotite mineral phases. We find spinel/melt partitioning of  $\text{Fe}_2\text{O}_3$  ( $D_{\text{Fe}_2\text{O}_3}^{\text{spl}/\text{melt}}$ ) increases as spinel  $\text{Fe}_2\text{O}_3$  concentrations increase, independent of increases in  $f_{\text{O}_2}$ , and decreases with temperature, which is consistent with new and previous experiments at 0.1 MPa. We find  $D_{\text{Fe}_2\text{O}_3}^{\text{opx}/\text{melt}} = 0.63 \pm 0.10$  and  $D_{\text{Fe}_2\text{O}_3}^{\text{cpx}/\text{melt}} = 0.78 \pm 0.30$ . MORB  $\text{Fe}_2\text{O}_3$  and  $\text{Na}_2\text{O}$  concentrations are consistent with a modeled MORB source with  $\text{Fe}_2\text{O}_3 = 0.48 \pm 0.03$  wt% ( $\text{Fe}^{3+}/\Sigma\text{Fe} = 0.053 \pm 0.003$ ) at potential temperatures ( $T_p$ ) from 1320 to 1440 °C. The temperature-dependence of the  $D_{\text{Fe}_2\text{O}_3}^{\text{spl}/\text{melt}}$  function alone allows ~40% of the variation in MORB compositions. If we allow  $D_{\text{Fe}_2\text{O}_3}^{\text{opx}/\text{melt}}$  and  $D_{\text{Fe}_2\text{O}_3}^{\text{cpx}/\text{melt}}$  to also vary with temperature by tying them to spinel  $\text{Fe}_2\text{O}_3$  through intermineral partitioning, then all the MORB data are within error of the model. Our model  $\text{Fe}_2\text{O}_3$  concentration for the MORB source would require that the convecting mantle be more oxidized at a given depth than recorded by continental mantle xenoliths. Our result is supported by thermodynamic models of mantle with  $\text{Fe}^{3+}/\Sigma\text{Fe} = 0.03$  that predict  $f_{\text{O}_2}$  of ~QFM-1 near the garnet-spinel transition, which is inconsistent with  $f_{\text{O}_2}$  of MORB. Our results support previous suggestions that redox melting may occur between 200 and 250 km depth.

**Keywords** MORB · Oxygen fugacity · Experimental petrology · Mantle petrology

## Introduction

Estimates of upper mantle oxygen fugacity ( $f_{\text{O}_2}$ ) and the bulk ferric iron content of the upper mantle inform petrological and geophysical models of the mantle. For example, the depth of redox melting in the mantle will be deeper if the mantle is more oxidized (Dasgupta et al. 2013; Stagno et al. 2013), potential temperatures inferred from magma

compositions are lower under more oxidized conditions (Herzberg and Asimow 2008; Asimow 2021), and increased olivine ferric concentrations and associated defects may reduce seismic wave velocities and increase seismic attenuation (Cline II et al. 2018). The absence of a deep xenolith record from the convecting mantle forces workers to assume that the continental xenolith record (e.g., Frost and McCammon, 2008) can stand in for the  $f_{\text{O}_2}$ -depth profile of the convecting oceanic upper mantle; however, the absence of a deep xenolith record from the convecting mantle prevents evaluation of this assumption or even any direct assessment of the  $f_{\text{O}_2}$  of the unmelted oceanic upper mantle. This shortfall in the geologic record highlights the importance of ridge  $f_{\text{O}_2}$  as an anchor for modeling  $f_{\text{O}_2}$  deeper in the convecting mantle.

Although key for understanding  $f_{\text{O}_2}$  at depth,  $f_{\text{O}_2}$  measurements of MORB (Christie et al. 1986; Bézous and Humler 2005; Cottrell and Kelley 2011; Berry et al. 2018; O'Neill

Communicated by Dante Canil.

✉ Fred A. Davis  
fdavis@d.umn.edu

<sup>1</sup> Department of Earth and Environmental Sciences, University of Minnesota Duluth, 229 Heller Hall, 1114 Kirby Drive, Duluth, MN 55812, USA

<sup>2</sup> National Museum of Natural History, Smithsonian Institution, Washington, DC 20560, USA

et al. 2018; Zhang et al. 2018) and ridge peridotites (Bryndzia and Wood 1990; Birner et al. 2018) cannot be directly related to the  $f_{O_2}$  of unmelted, convecting upper mantle. Even correcting for the effects of depressurization upon ascent, which are well-characterized for ascending melts (Kress and Carmichael 1991) but poorly understood for peridotites (Birner et al. 2018), does not account for the redistribution of  $Fe_2O_3$  between minerals and melt during partial melting and melt extraction.

The  $f_{O_2}$  of MORB, and their  $Fe^{3+}/\Sigma Fe$  ratios when corrected for crystal-fractionation, span a relatively narrow range and appear insensitive to variations in extent of melting or mantle temperature (Bézos and Humler 2005; Cottrell and Kelley 2011; O'Neill et al. 2018). Possible reasons for this include reactions that limit changes in  $f_{O_2}$  as peridotites undergo partial melting (Davis and Cottrell 2018; Sorbadere et al. 2018) or buffering by the presence of sulfides in the MORB source (Cottrell and Kelley 2011). In contrast,  $Fe_2O_3$  does show systematic variations in MORB, which may provide a clue to what processes affect redox during MORB generation. If  $Fe_2O_3$  in the MORB source could be modeled as an incompatible element with a static bulk partition coefficient, then  $Fe_2O_3$  and  $Na_2O$  in MORB at an  $MgO$  concentration of 8 wt% should correlate positively. Observing the opposite in MORB, Bézos and Hummer (2005) suggested that  $Fe_2O_3$  could not be modeled using simple mineral/melt partitioning. Cottrell and Kelley (2011) confirmed a negative correlation between  $Fe_2O_3(8)$  and  $Na_2O(8)$  and suggested that it could be explained if bulk  $Fe_2O_3$  partitioning varied strongly as a function of mantle potential temperature ( $T_p$ ). The suggestion being that, while  $Fe_2O_3$  cannot be modeled by a single partition coefficient, inversion of the partial melting process may be achievable with knowledge of  $Fe_2O_3$  mineral/melt partition coefficients over a range of conditions and compositions. Experimental measurements of  $Fe_2O_3$  partition coefficients are few (McCanta et al. 2004; Mallmann and O'Neill 2009; Davis and Cottrell 2018; Sorbadere et al. 2018). Testing Cottrell and Kelley's (2011) mechanism for MORB  $Fe_2O_3$  systematics requires experiments under mantle pressures and temperatures at variable  $f_{O_2}$  and techniques for measuring  $Fe_2O_3$  in the experimental melts and minerals. Only then will we be able to invert ridge  $f_{O_2}$  measurements into measurements of convecting upper mantle  $f_{O_2}$ .

Unfortunately, controlling oxygen fugacity in solid-media, high-pressure experiments at the moderate  $f_{O_2}$  appropriate to Earth's mantle is difficult. The conventional approach to controlling  $f_{O_2}$  in a solid-apparatus employs graphite; however, this limits the  $f_{O_2}$  to below the graphite- $CO_2$  buffer (Holloway et al. 1992). If MORB source  $f_{O_2}$  were consistent with graphite saturation, as once believed (Christie et al. 1986; Blundy et al. 1991; Ballhaus 1993), graphite capsules would serve as ideal containers. It is now widely recognized, however, that MORB chemistry is inconsistent

with graphite saturation in the mantle, because basalts and peridotites record more oxidized conditions near the quartz-fayalite-magnetite (QFM) buffer (Cottrell and Kelley 2011; Birner et al. 2018; O'Neill et al. 2018; Zhang et al. 2018) and because carbon behaves incompatibly during MORB genesis (Hauri et al. 2019). The  $f_{O_2}$  enforced by graphite capsules is much lower than conditions in the MORB source region (Fig. 1).

To vary  $f_{O_2}$  at high pressure or to access  $f_{O_2}$ s more comparable to the MORB source, experimentalists can enforce discrete  $f_{O_2}$ s defined by metal-oxide buffers, such as nickel-nickel oxide (NNO), so long as  $f_{H_2O}$  of the buffer equals  $f_{H_2O}$  of the sample or  $f_{H_2O}$  within the capsule can be calculated (Eugster 1957; Blatter et al. 2013). Because this technique requires saturation in a hydrous fluid, it is an unsatisfying method of  $f_{O_2}$  control when the system of interest is nominally anhydrous, as is true for magma genesis at ridges.

Here, we describe and apply a new technique for controlling  $f_{O_2}$  in anhydrous experiments by encapsulating experiments in Pt-Fe alloy capsules, which we have used to saturate basaltic melts in several mantle minerals at  $f_{O_2}$  between QFM + 0.25 and QFM + 3 at 1.5 GPa. The technique combines the method of estimating equilibrium melt and alloy compositions developed by Kessel et al. (2001) with a method for pre-saturating Pt-Fe alloy capsules used by Ford (1978). We additionally performed more reduced experiments at about QFM-3 in graphite capsules, and we performed experiments at 0.1 MPa near QFM at 1300 and 1400 °C to isolate effects of temperature on spinel–melt partitioning of  $Fe_2O_3$ . We measured  $Fe^{3+}/\Sigma Fe$  ratios of

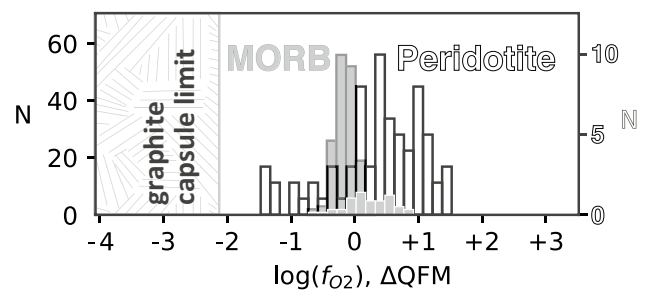


**Fig. 1** The histogram of  $f_{O_2}$  calculated from MORB (dark gray histogram) and ridge peridotite (white histogram) chemistries reported in the literature is modified from Cottrell et al. (2021) and includes MORB  $f_{O_2}$ s reported by O'Neill et al. (2018) in light gray. The  $f_{O_2}$  values are not projected back to mantle source conditions but are calculated at erupted temperature of 1200 °C at 0.1 MPa for basalts (Cottrell and Kelley 2011) and olivine-spinel thermometry temperatures at 0.6 GPa for peridotites (Birner et al. 2018). Left-side y-axis shows the number of MORB samples and the right-side y-axis shows the number of peridotite samples. The cross-hatched field shows  $f_{O_2}$  imposed by graphite capsules. Graphite capsule limit  $f_{O_2}$  is for silicate melts and was estimated by calculating  $f_{O_2}$  of a silicate liquid with 5 wt% dissolved  $CO_2$  at pressure and temperature range 1–3 GPa and 1200–1450 °C using equation 14 of Stagno and Frost (2010)

experimental glasses and spinels and calculated indirectly the  $\text{Fe}_2\text{O}_3$  concentrations of the experimental pyroxenes in equilibrium with olivine. We used these partition coefficients, derived from experiments on mantle-like compositions under relevant pressures and temperatures, and results from the literature, in simple forward models of MORB genesis. Our results suggest that  $\text{Fe}_2\text{O}_3$ - $\text{Na}_2\text{O}$  systematics in MORB can be accounted for by variations in  $\text{Fe}_2\text{O}_3$  partitioning with temperature. Bulk  $\text{Fe}_2\text{O}_3$  in the MORB source required to match the model to observations in MORB suggest the MORB source may be richer in  $\text{Fe}_2\text{O}_3$  than previously thought.

## Experimental and analytical methods

### Piston cylinder experiments

Using data from Kessel et al. (2001), we equilibrated Pt tubing with magnetite in a gas-mixing furnace to achieve specific Pt-Fe alloy compositions, such that our capsules were already in near-equilibrium with our melts at the  $f_{\text{O}_2}$  targeted in our high pressure and temperature runs. We prepared the tubing using methods adopted from Ford (1978). We cut 2-mm outer diameter, 1.4 mm inner diameter Pt tubing into 4.5–6 mm lengths. These tubes were packed and surrounded with a mixture of 70% by weight reagent grade magnetite and 30% sodium metasilicate ( $\text{Na}_2\text{SiO}_3$ ), which allowed wetting of the capsule by a melt that acted as the transfer medium for Fe while maintaining saturation in magnetite. We suspended the tubes in Pt boats at 0.1 MPa and at the appropriate T- $f_{\text{O}_2}$  conditions to achieve our desired alloy composition (pre-saturation conditions are given in Supplementary Table S1).

After pre-saturation, we dissolved the mixture of magnetite and silicate glass from the tube by bathing in warm hydrofluoric or hydrochloric acid for 24–48 h. We coned, sealed, and flattened each end of the tube loaded with starting materials. We also ran experiments in graphite-lined 4-mm Pt capsules so that we would have experimental runs under relatively reducing conditions for comparison.

We designed our starting materials to begin with a base residue composition, SPR-1, which had a bulk composition roughly equivalent to a mixture of olivine, orthopyroxene (opx), clinopyroxene (cpx), and spinel in the proportions 30:30:30:10. We based the individual mineral compositions in this mixture on the residual minerals of fertile peridotite partial melting experiment MPY #39 of Robinson et al. (1998), adding Fe only as FeO. To this base composition, we added a powder representative of the melt phase in proportions intended to produce an experimental melt fraction of about 70%, and all  $\text{Fe}_2\text{O}_3$  added to the experiments was added as a part of these mixtures. Experiments PC105-107

contained only the melt mixture with no peridotite residue component.

The starting materials were mixtures of reagent grade oxides and carbonates ( $\text{SiO}_2$ ,  $\text{TiO}_2$ ,  $\text{Al}_2\text{O}_3$ ,  $\text{Cr}_2\text{O}_3$ ,  $\text{Fe}_2\text{O}_3$ , FeO,  $\text{MnCO}_3$ , MgO,  $\text{CaCO}_3$ ,  $\text{Na}_2\text{CO}_3$ ,  $\text{K}_2\text{CO}_3$ ). We doped most of these experiments with a mixture of first-row transition elements at a concentration of about 100 ppm each (Sc, V, Co, Ni, Zn, Ga, Ge). We mixed each starting composition over several steps. During each mixing step, we homogenized powders by grinding in an agate mortar and pestle under ethanol for 30 min to an hour. Before adding FeO and  $\text{Fe}_2\text{O}_3$ , we decarbonated the starting mixtures in a muffle furnace at 1000 °C overnight. We weighed powders before and after decarbonation to check that all carbon had been removed from the powders. Compositions of the starting materials are in Supplementary Table S2.

We performed high-pressure experiments in a Rockland Research end-loaded piston cylinder apparatus at the Smithsonian Institution National Museum of Natural History with a ½" pressure vessel. Assemblies comprised MgO spacers, a straight-walled graphite furnace,  $\text{BaCO}_3$  pressure sleeves, and an outer layer of Pb foil. We controlled temperature to within  $\pm 10$  °C using type-D thermocouple. Positions of the capsule and thermocouple are equidistant from the furnace hotspot. Friction correction required for the  $\text{BaCO}_3$  assembly on this piston cylinder device was tested using falling Pt spheres in NaCl to find the melting point of NaCl. The resulting friction correction matches that of Fram and Longhi (1992).

We mounted experimental assemblies in epoxy, vertically sectioned them, and polished them for electron microprobe analysis. We also wafered samples to approximately 100  $\mu\text{m}$  thickness for analysis by X-ray absorption near-edge structure spectroscopy (XANES). We give additional details of the experimental design and methods in the Supplement and the run conditions of all experiments can be found in Table 1.

### 0.1 MPa gas-mixing experiments

We performed experiments at 0.1 MPa, 1306 and 1400 °C, and  $f_{\text{O}_2}$  of QFM + 0.6 (Table 1) in a Del-Tech vertical gas-mixing furnace at the Smithsonian Institution National Museum of Natural History. We controlled  $f_{\text{O}_2}$  to within  $\pm 0.05$  log units using a mix of CO and  $\text{CO}_2$  gas and monitored  $f_{\text{O}_2}$  during the experiment using a  $\text{ZrO}_2$ -Pt oxygen sensor, referenced to air. We calibrated the sensor against a gas mixture of 50% CO, 50%  $\text{CO}_2$ . We monitored temperature inside the furnace tube using a PtRh thermocouple and controlled to within  $\pm 2$  °C of 1225 °C. The thermocouple was calibrated against the melting point of Au wire. Experimental charges were hung from Pt-loops by mixing starting powders with polyvinyl alcohol and

**Table 1** Experimental run conditions

Expt #	Starting mix	P (GPa)	T (°C)	Pt-Fe capsule # <sup>2</sup>	Phase assemblage	Preferred $f_{O_2}$ relative to QFM <sup>1</sup>	Err	% Relative change in Fe	Err
Melt with no added residue—capsule meant fo QFM+1									
PC105	SPR-1 Melt QFM+1	1.5	1350	8	glass + spl + cpx + grt	+2.13	±0.65	-20	±5.5
PC106	SPR-1 Melt QFM+1	1.5	1380	9	glass + spl	+2.13	±0.65	-20.5	±1.7
PC107	SPR-1 Melt QFM+1	1.5	1370	10	glass + spl + cpx	+2.1	±0.65	-26.6	±3.2
Graphite capsule									
PC128	SPR-1 Mix Graphite	1.5	1380	N/A	glass + spl + opx			-5.2	±2.3
PC130	SPR-1 Mix Graphite	1.5	1350	N/A	glass + spl + opx + cpx			-9.4	±6.2
PC216	SPR-1 Mix2 Graphite	1.5	1380	N/A	glass + spl + ol + opx + cpx	-2.85	+1.21, -2.86	-10.1	±1.9
Capsule meant for QFM-1									
PC256	SPR-1 mix1 QFM-1	1.5	1380	60	qnch + spl + ol + opx + cpx	+1.48	±0.44		
PC261	SPR-1 mix3 QFM-1	1.5	1380	63	glass + spl + ol + opx + cpx	+1.29	±0.45	-20.1	±5.7
Capsule meant for QFM									
PC112	SPR-1 Mix QFM	1.5	1380	18	glass + spl + opx + cpx	+0.84	±0.65	-19.1	±5.1
PC126	SPR-1 Mix2 QFM+1	1.5	1380	23	glass + spl + ol + opx + cpx	+0.25	±0.50	-12.1	±2.2
Capsule meant for QFM+1									
PC108	SPR-1 Mix QFM+1	1.5	1380	11	glass + spl + opx + cpx	+2.04	±0.65	-26.8	±5.5
PC109	SPR-1 Mix2 QFM+1	1.5	1380	13	glass + spl + ol + opx	+1.51	±0.48	-28.7	±3.7
PC110	SPR-1 Mix2 QFM+1	1.5	1380	16	glass + spl + ol + opx + cpx	+0.85	±0.49	-22.9	±6.5
PC124	SPR-1 Mix3 QFM+1	1.5	1380	14	glass + spl + opx	+1.65	±0.65	-49.2	±1.3
PC127	SPR-1 Mix2 QFM+1	1.5	1380	26	glass + spl + ol + opx	+1.26	±0.47	-19.8	±3.3
PC231	SPR-1 Mix5 QFM+1	1.5	1380	50	glass + spl + ol + opx + cpx	+1.66	±0.43	-6.8	±7.4
Capsule meant for QFM+2									
PC242	SPR-1 Mix1 QFM+2	1.5	1380	58	glass + spl + ol + opx + cpx	+3.01	±0.44	-6.6	±7.2
PC247	SPR-1 Mix1 QFM+2	1.5	1400	57	glass + spl + ol + opx + cpx	+2.8	±0.45	-13.9	±2.7
0.1 MPa experiments									
SpCr1300	CrSpl1300	0	1306		glass + spl	+0.53	±0.05		
SpCr1400	CrSpl1400	0	1400		glass + spl	+0.60	±0.05		

<sup>a</sup>Preferred  $f_{O_2}$  in piston cylinder experiments is determined by spinel-olivine-opx equilibrium when those phases were present and alloy-melt equilibrium otherwise. Preferred  $f_{O_2}$  in the 0.1 MPa experiments is the  $f_{O_2}$  of the gas-mix measured by ZrO<sub>2</sub>-Pt oxygen sensor

<sup>b</sup>Furnace conditions for capsule pre-saturation given in Supplemental Table S15

partially fusing in air at 1400 °C. Each Pt loop was pre-saturated in Fe by equilibrating with experimental starting powder at the run temperature and gas mix of each experiment for 24 h. After pre-saturation, run products were removed from the loops by soaking in hydrofluoric acid overnight. Pt loops were then reloaded with starting powder and hung in the furnace under the conditions given in Table 1. We quenched experiments by dropping the loop into a water bath without exposing the samples or gas mix in the furnace to air. We mixed starting compositions from

reagent-grade oxides as described above for piston cylinder experiments.

## Analytical methods

### Electron probe microanalysis (EPMA)

We analyzed experimental phases for major elements by wavelength dispersive spectrometry (WDS) using a JEOL 8900 Superprobe and a JEOL JXA-8530F Hyperprobe

field-emission gun electron microprobe at the Smithsonian Institution. When analyzing spinels, we also analyzed a set of spinel standards with  $\text{Fe}^{3+}/\Sigma\text{Fe}$  ratios previously determined by Mössbauer spectroscopy (Bryndzia and Wood 1990; Ionov and Wood 1992; Wood and Virgo 1989 now available from the Smithsonian Institution with NMNH catalog # 118320), allowing accurate determination of spinel chemistry (Davis et al. 2017). We provide EPMA details and standards used in Supplementary text and Supplementary Table S3.

### X-ray absorption near-edge structure (XANES) analysis of $\text{Fe}^{3+}/\Sigma\text{Fe}$ ratios in glass

We measured  $\text{Fe}^{3+}/\Sigma\text{Fe}$  ratios in experimental glasses using Fe-XANES at station 13-ID-E at the Advanced Photon Source (APS), Argonne National Laboratory, USA., following the method of Cottrell et al. (2009) modified to mitigate beam damage (Cottrell et al. 2018). We prepared samples to a thickness of about 100  $\mu\text{m}$ .

We calculated  $\text{Fe}^{3+}/\Sigma\text{Fe}$  ratios in the glass from the centroids of the pre-edge doublet and using the basalt standard glasses of Cottrell et al. (2009) and the calibration curve of Zhang et al. (2018). Standard glass LW\_0 was analyzed repeatedly throughout each analytical session and we corrected pre-edge centroid energies such that the centroid of LW\_0 (Cottrell et al. 2009) was 7112.3 eV. In addition to choosing optically clear glass for analysis, we also examined all spectra for evidence of crystal interference and discarded any spectra with unusual short-range order. XANES spectral data are given in Supplementary Table S4.

Experiments in graphite returned  $\text{Fe}^{3+}/\Sigma\text{Fe}$  ratios below the detection limit with XANES (near QFM-2.5, Cottrell and Kelley, 2011). We have calculated glass  $\text{Fe}^{3+}/\Sigma\text{Fe}$  ratios from PC216 using Eq. 7 of Kress and Carmichael (1991) and  $f_{\text{O}_2}$  calculated from spinel-olivine-opx equilibrium.

### Calculation of $f_{\text{O}_2}$

We calculated  $f_{\text{O}_2}$  for the experimental assemblages by three independent methods (Supplementary Table S5). In all cases, when we give  $f_{\text{O}_2}$  relative to the quartz-fayalite-magnetite buffer (QFM), we calculate the buffer using the formulation of Frost (1991). When spinel, olivine, and orthopyroxene were all present, we calculated  $f_{\text{O}_2}$  from the equilibrium between these phases (Mattioli and Wood 1988) following the method described by Davis et al. (2017). When a large glass pool was available, we calculated  $f_{\text{O}_2}$  from the glass composition, deriving the  $\text{Fe}^{3+}/\Sigma\text{Fe}$  ratio of the glass from Fe-XANES and applying the algorithm of Kress and Carmichael (1991). In most experiments, we were also able to calculate  $f_{\text{O}_2}$  from the equilibrium between the Pt-Fe alloy capsule and melt.

To calculate alloy-melt  $f_{\text{O}_2}$ , we calculated the activity coefficient of Fe in the alloy using Eq. 11a of Kessel et al. (2001) and included a pressure term described in the Supplementary text. We calculated  $\log f_{\text{O}_2}$  using Eqs. 3 and 4 of Médard et al. (2008). We also calculated  $\log f_{\text{O}_2}$  of this reaction using the  $\Delta G_{\text{rxn}}$  from Holzheid et al. (1997) with a pressure term added using the molar volume of Fe metal (Robie et al. 1995) and FeO in silicate melt (Ghiorso and Kress 2004) and the activity coefficient for FeO in silicate melt ( $\gamma_{\text{FeO}}^{\text{liq}}$ ) from O'Neill and Eggins (2002). The two methods both rely on  $\Delta G_{\text{rxn}}$  from Holzheid et al. (1997), and so only differ in the calculation of  $\gamma_{\text{FeO}}^{\text{liq}}$ . We found that  $\log f_{\text{O}_2}$  of these two methods agree to within less than  $\pm 0.1$  log units (Supplementary Table S5).

### $\text{Fe}^{3+}$ in pyroxenes

We estimate the  $\text{Fe}^{3+}$  concentration in the pyroxenes from the change in the apparent  $\text{Fe}^{2+}$ -Mg exchange coefficient between coexisting pyroxenes and olivines as a function of  $f_{\text{O}_2}$ . Given the small range of temperatures and the limited compositional range of our experiments, we expect the true olivine-pyroxene  $\text{Fe}^{2+}$ -Mg exchange coefficients ( $K_D^{\text{Fe-Mg}} = [X_{\text{Fe}^{2+}}^{\text{ol}} X_{\text{Mg}}^{\text{pyx}}] / [X_{\text{Mg}}^{\text{ol}} X_{\text{Fe}^{2+}}^{\text{pyx}}]$ ) to be constant. Because we expect little  $\text{Fe}^{3+}$  in olivine but significant  $\text{Fe}^{3+}$  in pyroxenes, the apparent olivine-pyroxene  $K_D^{\text{Fe-Mg}}$ , in which all Fe is treated as  $\text{Fe}^{2+}$ , should decrease as a function of  $f_{\text{O}_2}$  because the  $\text{Fe}^{3+}$  concentration in the pyroxene should increase as  $f_{\text{O}_2}$  increases. The degree of deviation between the true  $K_D^{\text{Fe-Mg}}$  and  $K_D^{\text{Fe-Mg}}$  can be used to estimate the amount of  $\text{Fe}^{3+}$  in the pyroxene. Although indirect, this method has the potential to be more accurate than calculating  $\text{Fe}^{3+}$  from pyroxene stoichiometry, because it relies upon only the Fe and Mg measurements in each phase rather than being affected by the individual errors of every element in the analysis, which has been shown to be untenable for pyroxenes (Canil and O'Neill 1996).

## Results

### Experimental products, Fe-loss, $f_{\text{O}_2}$ , and approach to equilibrium

All experiments contained a glass or crystallized quench melt and spinel  $\pm$  olivine  $\pm$  opx  $\pm$  cpx. PC105, which did not have the SPR-1 residue added to its starting composition, yielded glass + garnet + spinel + cpx. All experiments contained large glass pools, similar to those pictured in Fig. 2, that allowed us to analyze glasses by EPMA and XANES at least 100  $\mu\text{m}$  away from crystals or quench mattes. Silicate

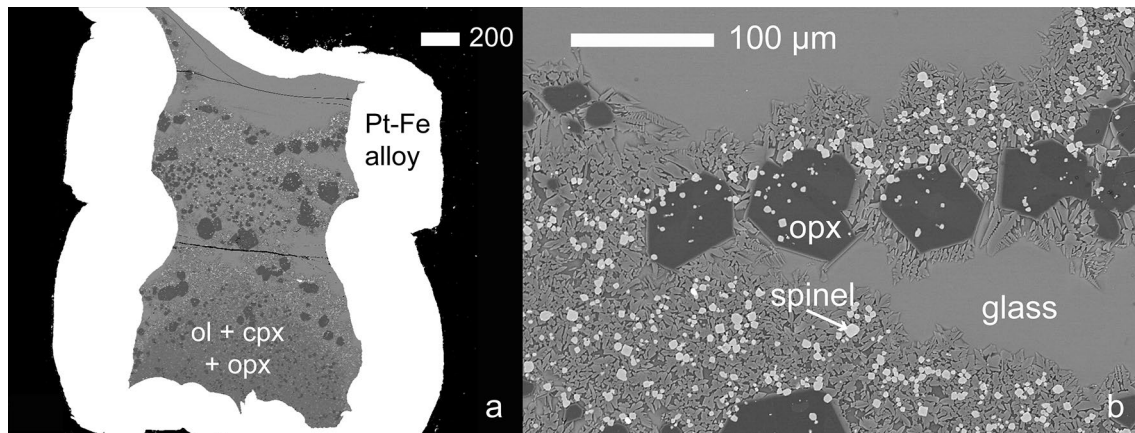


**Fig. 2** Back-scattered electron images of PC231 showing typical textures of the experimental phases. **a** Whole capsule image shows large glassy regions for XANES analysis, large opx surrounded by glass,

and smaller olivines and pyroxenes at the bottom. **b** View showing typical opx and spinel crystal sizes and textures and crystallized quenched melt texture nucleating on equilibrium opx and spinel

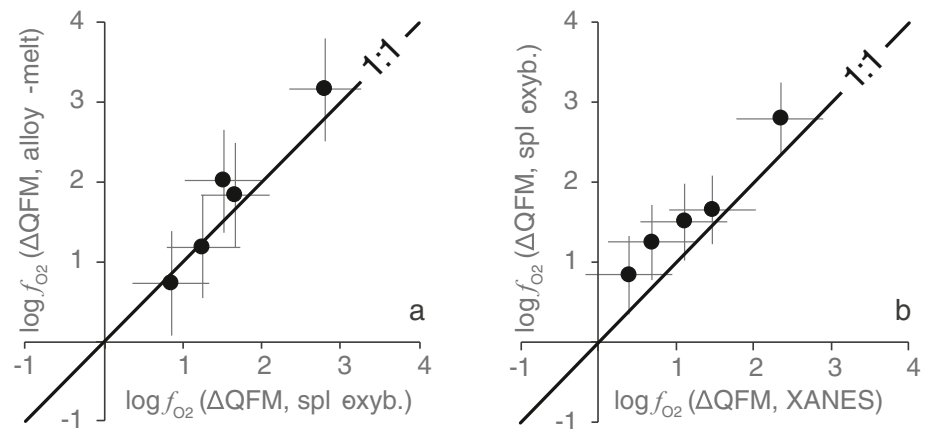
minerals had diameters between 10 and 180  $\mu\text{m}$  in most experiments (Fig. 2).

Mass balance indicates that experiments lost 5.7–49.2% of their total Fe to the capsule, though the majority lost less than 25% (Table 1 and Supplementary Table S6). Fe exchange with the capsule is probably unavoidable with this experimental design, and although we did not observe it, Fe-gain should be possible too. To meet some experimental objectives, Fe-loss must be strictly avoided (Grove 1981). In our case, Fe-loss did not compromise our experimental objectives, but did lead to adjustments to our experimental plan. Fe-loss led to an increase in bulk  $\text{Si}/(\text{Mg} + \text{Fe}^{2+})$ , which can cause the melt to become too silica rich to remain saturated in olivine. We did observe this phenomenon, and several of the experiments that lost a large fraction of their starting Fe did not stabilize olivine (Table 1). Starting compositions for experiments performed later in the series were informed by phase compositions of the earlier experiments, which allowed us to better predict the compositions of equilibrium phase assemblages at higher  $f_{\text{O}_2}$ . Diminished Fe-loss and consistent saturation in a four-phase solid residue in the higher numbered experiments (Table 1) are evidence that our ability to make these predictions improved. We considered whether Fe-loss could have led to disequilibrium between the experimental phases. Because the environment external to the capsule is Fe-poor, there is a sink that will continue to draw Fe out of the capsule over the entire course of the experiment and true equilibrium will never be reached (more information about the compositional profiles through the alloy capsules is given in the Supplement, in Supplementary Figure S1, and the compositions of the capsule interiors are given in Supplementary Table S7). But if the loss of Fe from the silicate to the capsule is slow compared to the time required for the silicate and oxide phases to reequilibrate, then equilibrium can be approached and  $\text{Fe}_2\text{O}_3$  partition

coefficients will still be equal to equilibrium values. Below we demonstrate that our experiments, including those with high degrees of Fe-loss, have approached redox and Fe equilibrium.

Several observations can be combined to demonstrate the experiments have made a close approach to equilibrium. One of the strongest pieces of evidence is the good agreement between different methods of calculating  $f_{\text{O}_2}$  from different phases. The three methods we used to calculate  $\log f_{\text{O}_2}$  all agree to within  $2\sigma$ . There is close agreement between  $f_{\text{O}_2}$  calculated from spinel-olivine-opx equilibrium and alloy-melt equilibrium (Fig. 3a), which agree to within  $1\sigma$  for all experiments where both methods could be applied. There is similarly close agreement between  $f_{\text{O}_2}$  calculated from spinel-olivine-opx equilibrium and XANES (Fig. 3b). Although all methods of calculating  $f_{\text{O}_2}$  agree to within  $2\sigma$ ,  $\log f_{\text{O}_2}$  calculated from XANES are systematically offset to lower  $\log f_{\text{O}_2}$  when compared to spinel-olivine-opx equilibrium by about 0.4 log units on average (Fig. 3b). Davis and Cottrell (2018) showed that these two methods agree, with no systematic offset, in experiments conducted on a basaltic andesite composition at 0.1 MPa. Although we do not know the reason for the systematic offset observed at high pressure, possible reasons include: (1) Eq. 7 in Kress and Carmichael (1991) underestimates the effect of pressure on  $f_{\text{O}_2}$ ; (2) Eq. 7 in KC91 underestimates  $f_{\text{O}_2}$  for this particular glass composition; (3) our Fe-XANES calibration, which is based on 0.1 MPa experiments, shifts with pressure. This last possibility seems unlikely because Zhang et al. (2017) collected Fe-XANES and Mössbauer spectroscopy data on high-pressure experimental andesite glasses and found that coordination number for  $\text{Fe}^{2+}$  increases with pressure, while coordination of  $\text{Fe}^{3+}$  is unaffected. This change in coordination suggests that the 0.1 MPa glass XANES calibration of Cottrell et al. (2009), modified by Zhang et al. (2018),

**Fig. 3** Comparison between methods of calculating  $f_{O_2}$  of the experiments in alloy capsules. See methods for details of the  $f_{O_2}$  calculations



would overestimate, not underestimate,  $Fe^{3+}/\Sigma Fe$  ratios in high-pressure glasses. We considered the possibility of beam damage, but beam damage during XANES analyses would lead to overestimation, not underestimation, of the  $Fe^{3+}/\Sigma Fe$  ratio (Cottrell et al. 2018). This leaves us with options (1) and (2), and potentially other issues we have not considered. We note that neither the pressure term deduced by O'Neill et al. (2006) nor the pressure term of Kress and Carmichael (1991) adequately models the high-pressure experiments conducted at the Ru-RuO<sub>2</sub> buffer (itself carrying uncertainty with pressure) by O'Neill et al. (2006) or Zhang et al. (2017), making option (1) plausible but difficult to test further. Option (2) is plausible, though application of the Borisov et al. (2018) algorithm for the relationship between composition and  $f_{O_2}$  applied to the experiments in this study results in a similar offset to the one shown in Fig. 3b. We conclude that the effect of pressure on  $Fe^{3+}/\Sigma Fe$  ratio bears further investigation, but given the excellent agreement overall amongst the three methods we have used to constrain  $f_{O_2}$  (XANES, Pt-Fe alloy, and spinel-oxybarometry), we can move forward with confidence in our analysis.

The close agreement between spinel-olivine-opx and alloy-melt equilibria gives us confidence that  $f_{O_2}$  is well-constrained in these experiments because these methods of calculating  $f_{O_2}$  are completely independent. Moreover, we infer a close approach to redox equilibrium because the crystalline silicate and oxide phases record the same  $f_{O_2}$  as the capsule-melt couple, despite their different kinetic limitations. The likeliest source of disequilibrium in the experiments would result from rapid loss of Fe from the melt to the capsule, which would raise  $f_{O_2}$  locally, and incomplete communication of the new  $f_{O_2}$  to the crystalline solids. Good agreement of these oxybarometers suggests that redox is communicated throughout the sample quickly compared to the rate of Fe-loss to the capsule, and  $f_{O_2}$  approaches equilibrium.

It is possible that the crystalline phases and melt-capsule couple could reach redox equilibrium without attaining equilibrium partitioning of FeO and Fe<sub>2</sub>O<sub>3</sub> between the crystalline and

melt phases. This could result in crystals with appropriate  $Fe^{3+}/\Sigma Fe$  ratios but too high  $\Sigma Fe$  to have equilibrated with a melt that lost Fe to the capsule. We think this is unlikely because there are crystal-chemical constraints that disallow Fe to change valence without either charge-balancing coupled substitutions or defect migration. However, to account for this possibility, we further demonstrate that  $Fe^{2+}$  equilibrium is approached between the melt and the silicate minerals by comparing the  $Fe^{2+}$ -Mg exchange coefficient between olivine and liquid ( $K_D^{Fe-Mg}$ ) to expected values. We report both liquid  $Fe^{3+}/\Sigma Fe$  ratios and olivine saturation in six experiments. Olivine-liquid  $K_D^{Fe-Mg}$  in those experiments varies from 0.330 to 0.347 (Table S8 and Fig. 4), well within the model error of  $0.31-0.32 \pm 0.03$  predicted by Toplis (2005). If mineral  $Fe^{3+}/\Sigma Fe$  ratios are a function of  $f_{O_2}$  and both  $f_{O_2}$  and FeO have approached equilibrium, then Fe<sub>2</sub>O<sub>3</sub> must have as well. Given this result, Fe<sub>2</sub>O<sub>3</sub> partition coefficients are likely near-equilibrium values even in our experiments that have lost significant Fe. We, therefore, present all our experimental data and include all measurements of Fe<sub>2</sub>O<sub>3</sub> partition coefficients in our analysis. In some instances, it is

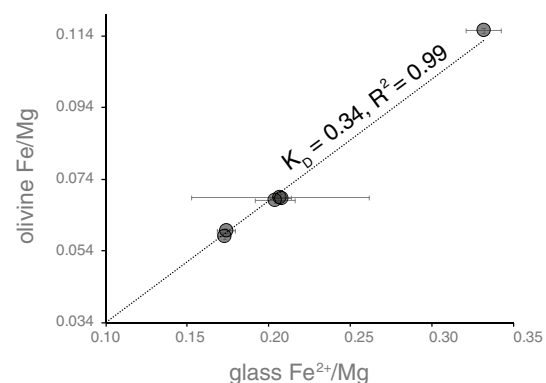


**Fig. 4** Olivine Fe/Mg plotted against glass  $Fe^{2+}/Mg$  for all experiments saturated in olivine where we were also able to measure  $Fe^{3+}/\Sigma Fe$  ratios of the glass. Black line is a linear fit through the origin showing that all our experiments are well-fit by a single value of olivine-liquid  $K_D^{Fe-Mg}$

useful to have the data from experiments with greater degrees of Fe-loss. For example, we will show below that spinel–melt partitioning of Fe<sub>2</sub>O<sub>3</sub> is dependent on the Fe<sub>2</sub>O<sub>3</sub> concentration of the spinel. We can distinguish the effect of Fe<sub>2</sub>O<sub>3</sub> concentration from the effect of *f*<sub>O<sub>2</sub></sub> because some experiments have both high *f*<sub>O<sub>2</sub></sub> and spinel with low Fe<sub>2</sub>O<sub>3</sub> concentration. This is possible because high *f*<sub>O<sub>2</sub></sub> experiments that experience high Fe-loss have spinels with oxidized Fe<sup>3+</sup>/ΣFe ratios while still having low Fe<sub>2</sub>O<sub>3</sub> because the experiment is low in total Fe.

Because we have multiple equilibria available to calculate *f*<sub>O<sub>2</sub></sub> in some experiments, we had to choose which methods we prefer for the purpose of plotting a single value for *f*<sub>O<sub>2</sub></sub> in our figures. Given the close agreement and independence of spinel-olivine-opx and alloy-melt oxybarometry, we adopt the spinel-olivine-opx *f*<sub>O<sub>2</sub></sub> as our preferred value of *f*<sub>O<sub>2</sub></sub> and alloy-melt *f*<sub>O<sub>2</sub></sub> when olivine was not present (Table 1 and Supplementary Table S5).

### Major element phase compositions

Major element compositions of the silicates glasses and minerals vary little over the > 4 log unit range in *f*<sub>O<sub>2</sub></sub>. Notable exceptions are a bimodality in SiO<sub>2</sub> and Al<sub>2</sub>O<sub>3</sub> concentrations between melts that crystallized olivine and those that did not and a range of variation in Mg# due to *f*<sub>O<sub>2</sub></sub>-driven variations in FeO and Fe-loss. Spinel vary in Cr# (Cr/[Al + Cr]) from 0.094 to 0.334. Spinel Fe<sup>3+</sup>/ΣFe ratios correlate strongly with log*f*<sub>O<sub>2</sub></sub> (*R*<sup>2</sup> = 0.685, *p* value < 0.0001) and range from 0.064 to 0.639. Average phase compositions are tabulated in Supplementary Tables S8–S12.

### Fe<sub>2</sub>O<sub>3</sub> in pyroxenes

Our method for estimating Fe<sub>2</sub>O<sub>3</sub> in pyroxenes relies on a correlation between the apparent olivine-pyroxene Fe–Mg exchange coefficients, which we notate as *K*<sub>D</sub><sup>Fe–Mg\*</sup> (in which we have treated all Fe as Fe<sup>2+</sup>) and log*f*<sub>O<sub>2</sub></sub>. Apparent *K*<sub>D</sub><sup>Fe–Mg\*</sup> between olivine and opx and between olivine and cpx are both significantly correlated with log*f*<sub>O<sub>2</sub></sub> relative to QFM (for opx: *R*<sup>2</sup> = 0.86, *p* value < 0.001; for cpx *R*<sup>2</sup> = 0.87, *p* value = 0.006; Fig. 5).

Having established that *K*<sub>D</sub><sup>Fe–Mg\*</sup> is a function of *f*<sub>O<sub>2</sub></sub>, we can estimate the concentration of Fe<sup>3+</sup> in the pyroxene by comparison with the “true” *K*<sub>D</sub><sup>Fe–Mg</sup>, in which only Fe<sup>2+</sup> is considered. If the true *K*<sub>D</sub><sup>Fe–Mg</sup> is known, then we can calculate Fe<sup>3+</sup> in pyroxene from the following equation:

$$X_{Fe^{3+}}^{pyx} = \frac{X_{Fe}^{ol} X_{Mg}^{pyx}}{X_{Mg}^{ol}} \left( \frac{1}{K_D^{Fe-Mg*}} - \frac{1}{K_D^{Fe-Mg}} \right), \tag{1}$$

where *X*<sub>*i*</sub><sup>*n*</sup> is the cations per formula unit (based on six oxygens for pyroxenes and four oxygens for olivine) of

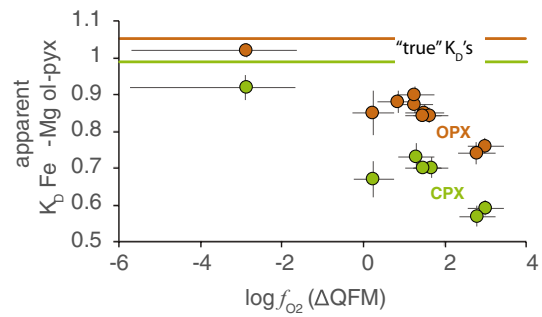


**Fig. 5** Apparent *K*<sub>D</sub><sup>Fe–Mg\*</sup> between olivine and pyroxene as a function of log *f*<sub>O<sub>2</sub></sub> (ΔQFM). *K*<sub>D</sub><sup>Fe–Mg\*</sup> is calculated by treating all Fe in olivine and pyroxene as Fe<sup>2+</sup>. Green circles are ol-cpx and orange circles are ol-opx pairs from this study. The trend to lower *K*<sub>D</sub><sup>Fe–Mg\*</sup> as *f*<sub>O<sub>2</sub></sub> increases indicates an increasing fraction of Fe<sup>3+</sup> in the pyroxenes. Lines for “true” *K*<sub>D</sub><sup>Fe–Mg</sup> show our estimate of the true *K*<sub>D</sub><sup>Fe–Mg</sup> if only Fe<sup>2+</sup> in the pyroxene were used to calculate it. We use “true” *K*<sub>D</sub><sup>Fe–Mg</sup> to calculate Fe<sub>2</sub>O<sub>3</sub> concentrations of the pyroxenes

cation *i* in phase *n*. Although true *K*<sub>D</sub><sup>Fe–Mg</sup> is likely close to the apparent value in the experiments performed in graphite, we leave open the possibility of significant Fe<sup>3+</sup> in those pyroxenes as well. Instead, we estimate the value of true *K*<sub>D</sub><sup>Fe–Mg</sup> by assuming that there is little enough Fe<sup>3+</sup> in the pyroxenes that the Fe<sup>3+</sup> pyroxene/melt partition coefficient will follow Henry’s law behavior; that is, we assume there will be a linear function describing the relationship between *X*<sub>Fe<sup>3+</sup></sub><sup>liq</sup> and *X*<sub>Fe<sup>3+</sup></sub><sup>pyx</sup> that passes through the origin. Using the relationship *X*<sub>Fe<sup>3+</sup></sub><sup>pyx</sup> = *D*<sub>Fe<sup>3+</sup></sub><sup>pyx/melt</sup> \* *X*<sub>Fe<sup>3+</sup></sub><sup>melt</sup> with Eq. 1 and rearranging terms, we were able to calculate true *K*<sub>D</sub><sup>Fe–Mg</sup>

through multiple linear regression. The resulting values are olivine-opx *K*<sub>D</sub><sup>Fe–Mg</sup> = 1.05 ± 0.02 and olivine-cpx *K*<sub>D</sub><sup>Fe–Mg</sup> = 0.99 ± 0.01. Our estimate of olivine-opx *K*<sub>D</sub><sup>Fe–Mg</sup> compares favorably with *K*<sub>D</sub><sup>Fe–Mg</sup> predicted from the equations of von Seckendorff and O’Neill (1993) of 1.11 ± 0.18, considering the large uncertainties of that model when the phases have high Mg# as do the experiments in our study. With these values, we can use Eq. 1 to calculate *X*<sub>Fe<sup>3+</sup></sub><sup>pyx</sup> for both opx and cpx in each experiment with coexisting olivine. Resulting Fe<sup>3+</sup>/ΣFe ratios vary from 0.03 ± 0.03 to 0.29 ± 0.04 in opx and 0.07 ± 0.05 to 0.43 ± 0.06 in cpx (Supplementary Table S13).

### Fe<sub>2</sub>O<sub>3</sub> partition coefficients

We use our measurements of Fe<sup>3+</sup>/ΣFe ratios in glass and spinel and our calculated Fe<sub>2</sub>O<sub>3</sub> concentrations in pyroxenes to estimate Fe<sub>2</sub>O<sub>3</sub> partition coefficients between minerals and melt and intermineral partition coefficients. We find that *D*<sub>Fe<sub>2</sub>O<sub>3</sub></sub><sup>sp/melt</sup> increases as a function of the Fe<sub>2</sub>O<sub>3</sub> concentration in the spinel (Fig. 6). As is required for the analysis above,

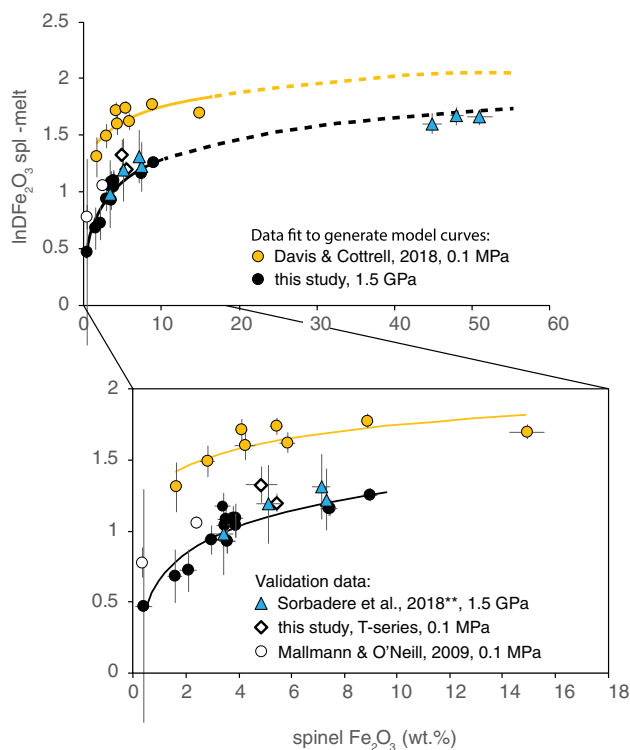


**Fig. 6** Spinel/melt partition coefficients measured in our experiments and experiments from the literature as a function of spinel  $\text{Fe}_2\text{O}_3$  concentration. Curves show best fits to data from this study and to data from Davis and Cottrell (2018) in the form  $\ln D_{\text{Fe}_2\text{O}_3}^{\text{spl/melt}} = a \ln C_{\text{Fe}_2\text{O}_3}^{\text{spl}} + b$

$\text{Fe}_2\text{O}_3$  concentrations in pyroxenes and melts are well-fit by a line through the origin. From the slope of these lines, we calculate average  $D_{\text{Fe}_2\text{O}_3}^{\text{opx/melt}} = 0.63 \pm 0.10$  and  $D_{\text{Fe}_2\text{O}_3}^{\text{cpx/melt}} = 0.78 \pm 0.30$  (Fig. 7). Mineral-melt partition coefficients calculated from each individual experiment are given in Supplementary Table S14.

## Discussion

### Comparisons with previous experiments

#### Spinel-melt partitioning of $\text{Fe}_2\text{O}_3$

There are several other experimental data sets we can compare to our measurements of  $D_{\text{Fe}_2\text{O}_3}^{\text{spl/melt}}$ . Mallmann and O'Neill (2009) performed experiments at 0.1 MPa and 1 GPa over a large range of  $f_{\text{O}_2}$  and fit functions for the partition coefficients of  $\text{Fe}^{2+}$  and  $\text{Fe}^{3+}$  between spinel and melt by assuming that functionally all Fe was  $\text{Fe}^{2+}$  in the most reduced experiments and  $\text{Fe}^{3+}$  in the most oxidized. Davis and Cottrell (2018) performed 0.1 MPa experiments and measured  $\text{Fe}^{3+}/\Sigma\text{Fe}$  ratios in glasses and spinels also equilibrated with olivine and opx. Sorbadere et al. (2018) presented  $D_{\text{Fe}_2\text{O}_3}^{\text{spl/melt}}$

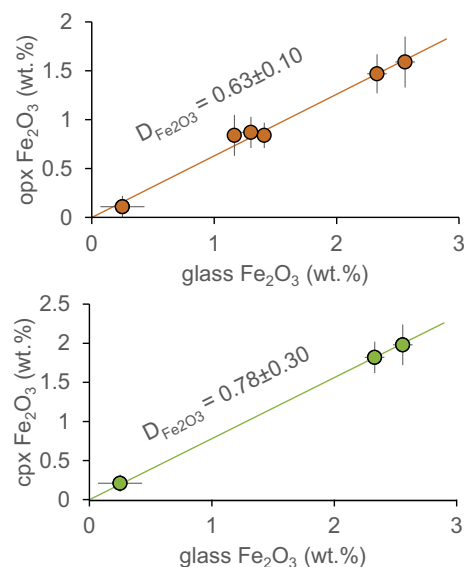


**Fig. 7**  $\text{Fe}_2\text{O}_3$  concentrations in glasses and coexisting pyroxenes. Values of  $D_{\text{Fe}_2\text{O}_3}^{\text{opx/melt}}$  and  $D_{\text{Fe}_2\text{O}_3}^{\text{cpx/melt}}$  were fit by linear regression through the origin

from a suite of 1.5 GPa piston cylinder experiments performed in graphite, Re, and AuPd capsules. Sorbadere et al. (2018) applied several methods to estimate  $f_{\text{O}_2}$  and, in contrast to this study, reported that the various methods disagreed by 1–7 log units within individual experiments; however, we recalculated  $f_{\text{O}_2}$  from their reported spinel, olivine, and opx analyses and found that the  $f_{\text{O}_2}$  they reported by spinel-olivine-opx oxybarometry is miscalculated, resulting in values of  $f_{\text{O}_2}$  too low by 2–3 log units in their Re1 and AuPd1 experiments. We plot the erroneous  $f_{\text{O}_2}$  reported by Sorbadere et al. (2018) and our recalculated values against their measured spinel  $\text{Fe}^{3+}/\Sigma\text{Fe}$  ratios in Supplementary Figure S2. For the purpose of comparing their results to ours, we have recalculated  $D_{\text{Fe}_2\text{O}_3}^{\text{spl/melt}}$  for the Sorbadere et al. (2018) experiments using  $f_{\text{O}_2}$  calculated from their spinel, olivine, and opx data following the same method we use for calculating  $f_{\text{O}_2}$  in our own experiments. We provide more details about recalculating the Sorbadere et al. (2018) data in the Supplement, and versions of our figures that include the reported partition coefficients of Sorbadere et al. (2018) can be found as Supplementary Figures S3 and S4.

Piston cylinder experiments in this study and 0.1 MPa experiments of Davis and Cottrell (2018) both show increasing  $D_{\text{Fe}_2\text{O}_3}^{\text{spl/melt}}$  with increasing  $\text{Fe}_2\text{O}_3$  concentrations in the spinel, but the two trends are offset with the new experiments at lower  $D_{\text{Fe}_2\text{O}_3}^{\text{spl/melt}}$  at a given spinel  $\text{Fe}_2\text{O}_3$  concentration (Fig. 6). Recalculated 1.5 GPa experiments from Sorbadere et al. (2018) plot along the same trend as our 1.5 GPa experiments. We can demonstrate that these two trends in

$D_{\text{Fe}_2\text{O}_3}^{\text{spl}/\text{melt}}$  are effects of  $\text{Fe}_2\text{O}_3$  concentration independent of  $f_{\text{O}_2}$  by comparing experiments at similar  $f_{\text{O}_2}$  but with different spinel  $\text{Fe}_2\text{O}_3$  concentrations. Experiments PC109 (QFM +  $1.51 \pm 0.48$ ) and PC231 (QFM +  $1.66 \pm 0.43$ ) record similar  $f_{\text{O}_2}$  but have different spinel  $\text{Fe}_2\text{O}_3$  concentrations ( $3.57 \pm 0.30$  wt% in PC109 and  $8.99 \pm 0.30$  wt% in PC231) and values of  $D_{\text{Fe}_2\text{O}_3}^{\text{spl}/\text{melt}}$  ( $2.53 \pm 0.22$  in PC109 and  $3.51 \pm 0.16$  in PC231). These experiments crystallized spinel with different  $\text{Fe}_2\text{O}_3$  concentrations at similar  $f_{\text{O}_2}$ , because PC109 experienced greater Fe-loss than PC231. Fe-loss decreases the  $\text{Fe}_2\text{O}_3$  concentration of the spinel and, consequently, the activity of magnetite. Nonetheless, high  $f_{\text{O}_2}$  in the solid assemblage is maintained, because Fe-loss also leads to an increase in the forsterite content of the olivine, which has significant leverage in the  $f_{\text{O}_2}$  calculation with higher forsterite contents corresponding to higher  $f_{\text{O}_2}$ .

The increase in  $D_{\text{Fe}_2\text{O}_3}^{\text{spl}/\text{melt}}$  with increasing spinel  $\text{Fe}_2\text{O}_3$  concentrations is clear in Fig. 6, but the reason for the offset between the 0.1 MPa and 1.5 GPa trends is not obvious. There are three major differences between the two sets of experiments that define these trends. The Davis and Cottrell (2018) experiments: (1) were performed at lower pressure (0.1 MPa v. 1.5 GPa), (2) were performed at lower temperature (1225 °C v. 1350–1400 °C), and (3) have spinels with greater Cr# (0.61–0.68 v. 0.09–0.33). We performed the 0.1 MPa experiments presented here to attempt to isolate some of these variables. Our new 0.1 MPa experiments are at the same pressure as the experiments we presented in Davis and Cottrell (2018) and also have similar Cr# = 0.61–0.67. The experiments are hotter than the experiments in Davis and Cottrell (2018), allowing us to test the effect of temperature at constant pressure and spinel composition (although, by necessity, there are still differences in the glass compositions). These two experiments show a trend of decreasing  $D_{\text{Fe}_2\text{O}_3}^{\text{spl}/\text{melt}}$  with increasing temperature from the 1225 °C experiments of Davis and Cottrell (2018) to the 1400 °C and 0.1 MPa experiment of this study (Fig. 8b).

We can further demonstrate that temperature is likely an important variable for  $D_{\text{Fe}_2\text{O}_3}^{\text{spl}/\text{melt}}$  using the experiments of Mallmann and O'Neill (2009). Their partition coefficients are fit to data from both 0.1 MPa and 1 GPa experiments, and there is no indication in their results that this pressure interval is important to  $D_{\text{Fe}_2\text{O}_3}^{\text{spl}/\text{melt}}$ . The Mallmann and O'Neill (2009) experiments were performed at 1300 °C, which is intermediate to the temperatures of experiments of Davis and Cottrell (2018) and the 1.5 GPa experiments of this study. The Cr# of the Mallmann and O'Neill (2009) spinels bracket the other available data. The Mallmann and O'Neill (2009) spinels show only a small difference in  $D_{\text{Fe}_2\text{O}_3}^{\text{spl}/\text{melt}}$  over a large range of spinel Cr# (Fig. 8a). This effect is not strong enough to explain the large difference in average  $D_{\text{Fe}_2\text{O}_3}^{\text{spl}/\text{melt}}$  between the experiments of Davis and Cottrell (2018) and

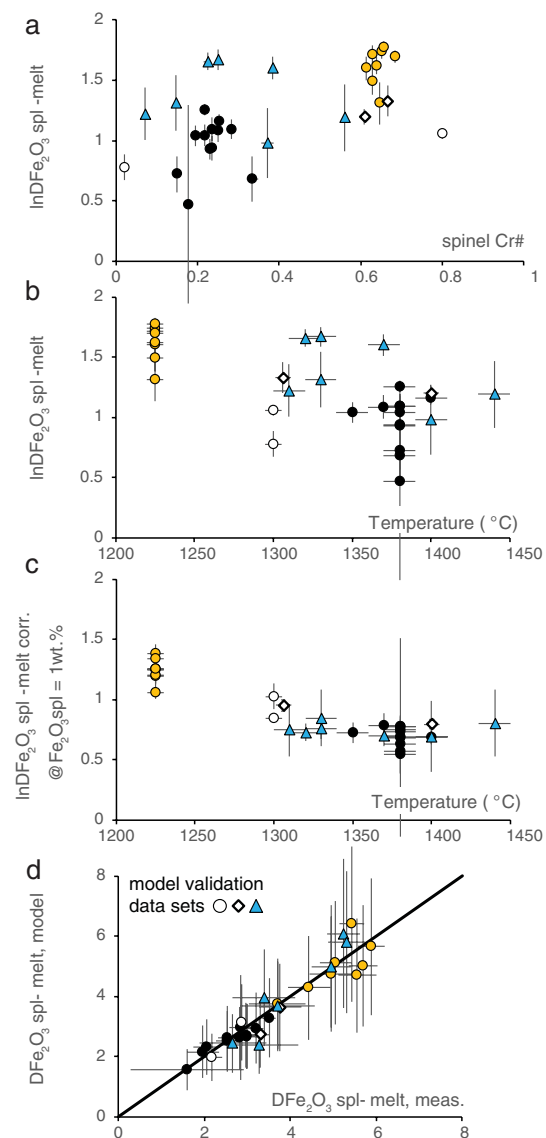


**Fig. 8** Experimental measurements of  $D_{\text{Fe}_2\text{O}_3}^{\text{spl}/\text{melt}}$  as a function spinel **a** Cr# and **b** temperature. **c**  $D_{\text{Fe}_2\text{O}_3}^{\text{spl}/\text{melt}}$  corrected to a common spinel  $\text{Fe}_2\text{O}_3$  concentration of 1 wt% using the coefficient for  $\ln(C_{\text{Fe}_2\text{O}_3}^{\text{spl}})$  from Eq. 4 to highlight the effect of temperature. **d**. Comparison between measured  $D_{\text{Fe}_2\text{O}_3}^{\text{spl}/\text{melt}}$  and modeled  $D_{\text{Fe}_2\text{O}_3}^{\text{spl}/\text{melt}}$  using Eq. 4. Data from this study and Davis and Cottrell (2018) were used to fit Eq. 4. Experiments from Mallmann and O'Neill (2009), Sorbadere et al. (2018), and our new 0.1 MPa experiments were not used to fit Eq. 4 and serve as validation of the model. Symbols are as in Fig. 6

this study. If we instead focus on the  $D_{\text{Fe}_2\text{O}_3}^{\text{spl}/\text{melt}}$  relationship to temperature, we see that the experiments of Mallmann and O'Neill (2009) have similar average  $D_{\text{Fe}_2\text{O}_3}^{\text{spl}/\text{melt}}$  to piston cylinder experiments in this study. The experiments in this study are 50–100 °C hotter; however, the effects of temperature are obscured in Fig. 8b, because the data plotted there span a large range of spinel  $\text{Fe}_2\text{O}_3$  concentrations, which

we have already shown has a strong effect on  $D_{\text{Fe}_2\text{O}_3}^{\text{spl}/\text{melt}}$ . After correcting for the effect of spinel  $\text{Fe}_2\text{O}_3$ , the temperature effect on  $D_{\text{Fe}_2\text{O}_3}^{\text{spl}/\text{melt}}$  becomes clearer (Fig. 8c). We note that the Sorbadere et al. (2018) experiments alone do not show a trend between  $D_{\text{Fe}_2\text{O}_3}^{\text{spl}/\text{melt}}$  and temperature after correcting for spinel  $\text{Fe}_2\text{O}_3$ ; however, there are two reasons why such a trend might be obscured in the Sorbadere et al. (2018) data. First, because we calculated  $\text{Fe}_2\text{O}_3$  in the glasses of these experiments from spinel oxybarometry, uncertainties in  $D_{\text{Fe}_2\text{O}_3}^{\text{spl}/\text{melt}}$  are greater than in our experiment with  $\text{Fe}_2\text{O}_3$  measured by XANES. Second, three of the Sorbadere et al. (2018) spinels have  $\text{Fe}_2\text{O}_3 > 40$  wt%, which is accompanied by dilution of  $\text{Cr}_2\text{O}_3$  and  $\text{Al}_2\text{O}_3$  compared to all the other experimental spinels. Although we have argued above that effects of spinel Cr# on  $D_{\text{Fe}_2\text{O}_3}^{\text{spl}/\text{melt}}$  are likely minor, we do not yet have sufficient data to determine whether spinel  $\text{Al}_2\text{O}_3$  and  $\text{Cr}_2\text{O}_3$  concentrations can have a significant effect on  $D_{\text{Fe}_2\text{O}_3}^{\text{spl}/\text{melt}}$  at extreme compositions like those in the most oxidized Sorbadere et al. (2018) spinels.

We modeled the effects of temperature and spinel  $\text{Fe}_2\text{O}_3$  concentration on  $D_{\text{Fe}_2\text{O}_3}^{\text{spl}/\text{melt}}$  empirically using the piston cylinder experiments from this study and experiments from Davis and Cottrell (2018). We excluded the Mallmann and O'Neill (2009) partition coefficients, the Sorbadere et al. (2018) partition coefficients, and our new 0.1 MPa partition coefficients from fitting so we could use those experiments for validation. We performed a multiple linear regression to fit coefficients  $a$ ,  $b$ , and  $c$  from the following function:

$$D_{\text{Fe}_2\text{O}_3}^{\text{spl}/\text{melt}} = a \frac{10000}{T} + b + c \ln\left(C_{\text{Fe}_2\text{O}_3}^{\text{spl}}\right), \quad (2)$$

where  $T$  is temperature in Kelvin and  $C_{\text{Fe}_2\text{O}_3}^{\text{spl}}$  is wt.% of  $\text{Fe}_2\text{O}_3$  in spinel. Fits are  $a = 0.87 \pm 0.07$ ,  $b = -4.6 \pm 0.4$ , and  $c = 0.24 \pm 0.02$ . The Mallmann and O'Neill (2009) partition coefficients, the recalculated Sorbadere et al. (2018) partition coefficients, and our 0.1 MPa partition coefficients are well-fit by the model (Fig. 8d) despite there being no model dependence on Cr or Al concentrations. Although, all the Mallmann and O'Neill (2009) experiments have low total Fe concentrations, there is a significant difference in total Fe between the high-Al and high-Cr groups, and it may be that the differences in  $D_{\text{Fe}_2\text{O}_3}^{\text{spl}/\text{melt}}$  between these groups are driven by differences in spinel  $\text{Fe}_2\text{O}_3$  concentration rather than Cr#. Additional experiments at varying spinel Cr#s are needed to better constrain the effects of other spinel compositional components on  $D_{\text{Fe}_2\text{O}_3}^{\text{spl}/\text{melt}}$ , but we are confident that Eq. 2 can be used to model  $D_{\text{Fe}_2\text{O}_3}^{\text{spl}/\text{melt}}$  under similar conditions to the experiments of this study, such as those that are pertinent to MORB generation.

## Pyroxene-melt partitioning of $\text{Fe}_2\text{O}_3$

We compare our  $D_{\text{Fe}_2\text{O}_3}^{\text{opx}/\text{melt}}$  and  $D_{\text{Fe}_2\text{O}_3}^{\text{cpx}/\text{melt}}$  to data from the literature (McCanta et al. 2004; Mallmann and O'Neill 2009; Rudra and Hirschmann 2019) in Fig. 9. In our experiments, there is no correlation between  $D_{\text{Fe}_2\text{O}_3}^{\text{opx}/\text{melt}}$  or  $D_{\text{Fe}_2\text{O}_3}^{\text{cpx}/\text{melt}}$  and  $f_{\text{O}_2}$ . There is no compelling evidence to suggest anything other than constant partition coefficients for both  $D_{\text{Fe}_2\text{O}_3}^{\text{opx}/\text{melt}}$  and  $D_{\text{Fe}_2\text{O}_3}^{\text{cpx}/\text{melt}}$  over the compositional range of our experiments and  $f_{\text{O}_2}$  between about QFM-3 and QFM+3 (Fig. 9).

## Comparing intermineral $\text{Fe}_2\text{O}_3$ partitioning to Mössbauer measurements of minerals in peridotite xenoliths

We also compare  $\text{Fe}_2\text{O}_3$  concentrations and intermineral partition coefficients to Mössbauer spectroscopy measurements of  $\text{Fe}_2\text{O}_3$  concentrations in minerals from spinel peridotite xenoliths (Dyar et al. 1989, 1992; McGuire et al. 1991; Luth and Canil 1993; Canil and O'Neill 1996; Woodland et al. 2006), which are more abundant than experiment measurements.  $\text{Fe}^{3+}/\Sigma\text{Fe}$  ratios in our experimental opx are higher than in the natural pyroxenes at a given  $f_{\text{O}_2}$ , while  $\text{Fe}^{3+}/\Sigma\text{Fe}$  ratios in our experimental cpx agree well with the natural data (Supplementary Figure S5a and b). Consequently, our experiments predict a slightly higher opx-cpx intermineral partition coefficient than the natural data (Supplementary Figure S5c).

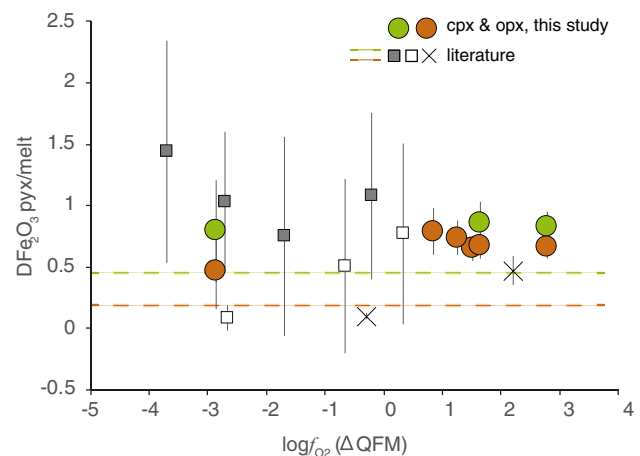


**Fig. 9** Experimental pyroxene/melt partition coefficients from this study and the literature. Green circles are cpx and orange circles are opx from this study. Squares are data from McCanta et al. (2004) pigeonite (gray) and augite (white). “X” symbols are pyroxenes from Rudra and Hirschmann (2019)

Woodland et al. (2006) investigated spinel-cpx inter-mineral partitioning of  $\text{Fe}_2\text{O}_3$  in xenoliths and found  $D_{\text{Fe}_2\text{O}_3}^{\text{spl/cpx}}$  increases with increasing spinel  $\text{Cr}/(\text{Cr} + \text{Al} + \text{Fe}^{3+})$  ratio. We do not observe a correlation between  $D_{\text{Fe}_2\text{O}_3}^{\text{spl/cpx}}$  and spinel  $\text{Cr}/(\text{Cr} + \text{Al} + \text{Fe}^{3+})$  ratio in our experiments (Supplementary Figure S6a).  $D_{\text{Fe}_2\text{O}_3}^{\text{spl/cpx}}$  in the xenolith data is also negatively correlated with cpx  $\text{Al}_2\text{O}_3$  concentration ( $R^2 = 0.40$ ,  $p$  value  $< 0.0001$ ; Fig. 10).  $D_{\text{Fe}_2\text{O}_3}^{\text{spl/cpx}}$  in our experiments is consistent with the relationship between  $D_{\text{Fe}_2\text{O}_3}^{\text{spl/cpx}}$  and cpx  $\text{Al}_2\text{O}_3$  concentration in the xenoliths, falling to the  $\text{Al}_2\text{O}_3$ -rich side of the trend (Fig. 10).

### Implications for $\text{Fe}_2\text{O}_3$ systematics in MORB lavas and MORB-source mantle

$\text{Fe}_2\text{O}_3$  and  $\text{Na}_2\text{O}$  in MORB corrected for crystal fractionation to a common  $\text{MgO}$  of 8 wt% ( $\text{Fe}_2\text{O}_3(8)$  and  $\text{Na}_2\text{O}(8)$ ) are negatively correlated, which is opposite the expected trend if  $\text{Fe}_2\text{O}_3$  could be treated simply as an incompatible element with a static partition coefficient (Bézos and Humler 2005; Cottrell and Kelley 2011).  $\text{Fe}^{3+}/\Sigma\text{Fe}$  ratios of MORB corrected for crystal fractionation do not correlate with  $\text{Na}_2\text{O}(8)$ , so that even as  $T_p$  and mean  $F$  of melting in the MORB source increase there is little change in the  $f_{\text{O}_2}$  of the melting region, similar to conclusions drawn from previous experimental studies of  $f_{\text{O}_2}$  and peridotite partial melting (Davis and Cottrell 2018; Sorbader et al. 2018). But what is the mechanism that allows  $f_{\text{O}_2}$  and melt  $\text{Fe}^{3+}/\Sigma\text{Fe}$  ratios to remain stable as melts are extracted? The negative correlation of  $\text{FeO}(8)$  with  $\text{Na}_2\text{O}(8)$  and with depth to the ridge axis have been attributed to variations in  $T_p$  (Klein and Langmuir 1987); that  $\text{Fe}_2\text{O}_3(8)$  is similarly correlated with  $\text{Na}_2\text{O}(8)$ ,

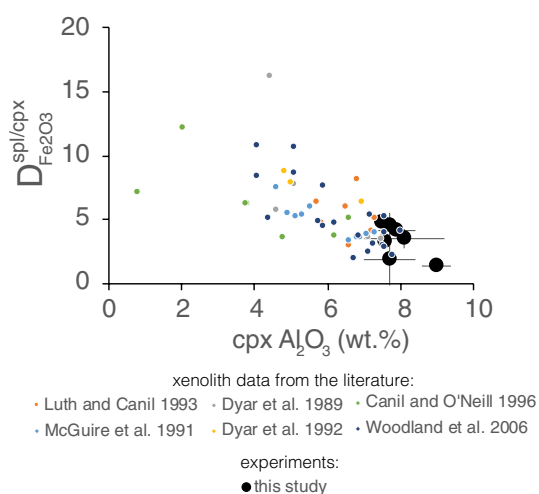


**Fig. 10**  $D_{\text{Fe}_2\text{O}_3}^{\text{spl/cpx}}$  from experiments in this study compared to  $D_{\text{Fe}_2\text{O}_3}^{\text{spl/cpx}}$  from xenoliths reported in the literature as a function of cpx  $\text{Al}_2\text{O}_3$  concentration

and indeed with  $\text{FeO}(8)$ , may indicate that temperature controls  $\text{Fe}_2\text{O}_3$  concentrations in primary MORB as well.

Cottrell and Kelley (2011) explored this idea with a forward melting model that used the mineral/melt partition coefficients of Mallmann and O'Neill, (2009) and compared their model to MORB data. They found that those partition coefficients could produce melts with  $\text{Fe}_2\text{O}_3(8)$  and  $\text{Na}_2\text{O}(8)$  concentrations similar to the average of the MORB array if the MORB-source mantle contained 0.37 wt%  $\text{Fe}_2\text{O}_3$ . Furthermore, they suggested the negative correlation between  $\text{Fe}_2\text{O}_3(8)$  and  $\text{Na}_2\text{O}(8)$  can be accounted for if the bulk partition coefficient for  $\text{Fe}_2\text{O}_3$  varied strongly as a function of temperature; however, insufficient data were available to test the magnitude of a temperature effect on bulk  $D_{\text{Fe}_2\text{O}_3}$ . With our new  $\text{Fe}_2\text{O}_3$  partition coefficients and our temperature-dependent equation for  $D_{\text{Fe}_2\text{O}_3}^{\text{spl/melt}}$  (Eq. 2), we can revisit this modeling approach. We note that using partition coefficients for  $\text{Fe}_2\text{O}_3$  is a fraught approach. Using a single bulk partition coefficient for  $\text{Fe}_2\text{O}_3$  and treating it as a trace element is certainly problematic; rigorous modeling of partial melting in the mantle requires maintaining redox equilibrium between residues and instantaneous partial melts. Thermodynamic models, such as the model of Jennings and Holland (2015), can treat mantle melting in this way, but it is not trivial for us to introduce our new findings about  $\text{Fe}_2\text{O}_3$  partitioning into that framework. Additionally, conditions of redox equilibrium between melt and residue are not maintained even in some of the most complex, popular, and successful thermodynamic models. For example, we have previously demonstrated that the MELTS family of models (Ghiorso and Sack 1995; Asimow and Ghiorso 1998; Ghiorso et al. 2002) generates residues and liquids that are far from redox equilibrium (Davis and Cottrell 2018). Ultimately, the amount of  $\text{Fe}_2\text{O}_3$  that enters mantle partial melts will still be governed by mineral–melt partition coefficients, assuming the absence of other significant redox couples (i.e., all the carbon is already oxidized). The following treatment works as a first approach to testing whether temperature-driven changes to  $\text{Fe}_2\text{O}_3$  partitioning are strong enough to account for variations observed in MORB and to estimate bulk  $\text{Fe}_2\text{O}_3$  in the MORB source; although, we hope to see our experimental results incorporated into thermodynamic models in the future.

We modeled  $\text{Fe}_2\text{O}_3$  and  $\text{Na}_2\text{O}$  concentrations of primary MORB melts by calculating bulk partition coefficients for  $\text{Fe}_2\text{O}_3$  and  $\text{Na}_2\text{O}$  assuming modal mineralogy of Depleted MORB Mantle (DMM) from Workman and Hart (2005). We used average values of  $D_{\text{Fe}_2\text{O}_3}^{\text{opx/melt}}$  and  $D_{\text{Fe}_2\text{O}_3}^{\text{cpx/melt}}$  from our experiments, calculated  $D_{\text{Fe}_2\text{O}_3}^{\text{spl/melt}}$  from Eq. 2, and used  $D_{\text{Fe}_2\text{O}_3}^{\text{ol/melt}}$  from Mallmann and O'Neill, (2009). We calculated  $D_{\text{Na}_2\text{O}}^{\text{cpx/melt}}$  from Eq. 16 of Blundy et al. (1995) and calculated  $D_{\text{Na}_2\text{O}}^{\text{opx/melt}}$  relative to  $D_{\text{Na}_2\text{O}}^{\text{cpx/melt}}$  from the inter-mineral partition coefficient

Na<sub>2</sub>O between opx and cpx from 1 and 1.5 GPa partial melting experiments (Supplementary Fig S7). Accumulated near-fractional melting calculations in pMELTS (Ghiorso et al. 2002) suggest that the 1380 °C average temperature of our experiments is similar to the mean temperature of isentropic melting of mantle with a potential temperature ( $T_p$ ) of 1400 °C. We calculated accumulated fractional melts at various melt fractions and source Fe<sub>2</sub>O<sub>3</sub> concentrations and corrected those melts for crystal fractionation for comparison to MORB glasses at 8 wt% MgO. We estimate 1 $\sigma$  uncertainties on model Fe<sub>2</sub>O<sub>3</sub>(8) at about 0.15 wt% and on model Na<sub>2</sub>O(8) at about 0.05 wt.% for each point along each of the modeled  $T_p$  curves. Additional details can be found in the Supplement.

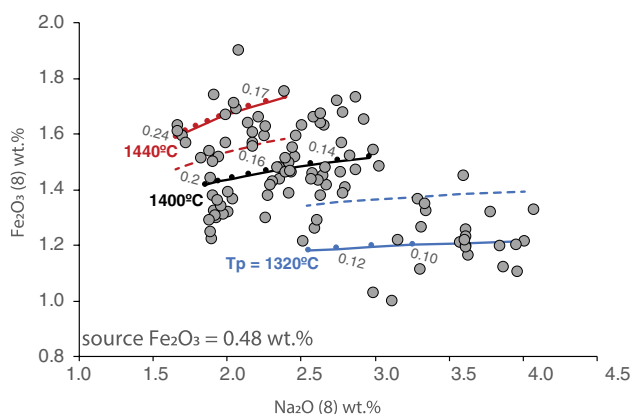


**Fig. 11** MORB glass Fe<sub>2</sub>O<sub>3</sub>(8) and Na<sub>2</sub>O(8) and forward-model melting curves are modified from Cottrell and Kelley (2011) using MORB data from Zhang et al. (2018), new data from this study, and a new modeling approach (described in the text). We corrected natural MORB glass compositions for crystal fractionation. We first corrected MORB with MgO > 8.5 wt% to MgO = 8.5 wt% by subtracting equilibrium olivine ( $K_D^{Fe-Mg} = 0.3$ ) and assuming perfect incompatibility of Na<sub>2</sub>O and Fe<sub>2</sub>O<sub>3</sub>. We then further corrected those compositions and the MORB glasses with MgO ≤ 8.5 wt% to MgO = 8 wt% using the equation of Klein and Langmuir (1987) Na<sub>2</sub>O(8) = Na<sub>2</sub>O + 0.373 \* MgO - 2.98 and the equation Fe<sub>2</sub>O<sub>3</sub>(8) = Fe<sub>2</sub>O<sub>3</sub> - 0.2391 \* (8 - MgO). In the Fe<sub>2</sub>O<sub>3</sub>(8) equation, -0.2391 is the slope of all the MORB glasses with MgO ≤ 8.5 wt% from Cottrell and Kelley (2011) with Fe<sup>3+</sup>/ΣFe ratios recalculated according to Zhang et al. (2018) in MgO-Fe<sub>2</sub>O<sub>3</sub> space. The solid black curve is for a source with bulk Fe<sub>2</sub>O<sub>3</sub> = 0.48 wt%,  $T_p = 1400$  °C, and for various melt fractions explored at 1% increments as indicated by tick marks on the model curves. Dashed curves show the effect of changing  $T_p$  to 1440 °C (red) or 1320 °C (blue) when  $D_{Fe_2O_3}^{spl/melt}$  and melt fraction are the only model inputs that change as a function of temperature. Dark red ( $T_p = 1440$  °C) and blue (1320 °C) curves show the effect of temperature for a source with bulk Fe<sub>2</sub>O<sub>3</sub> = 0.48 wt% when  $D_{Fe_2O_3}^{opx/spi}$  and  $D_{Fe_2O_3}^{cpx/spi}$  have a temperature dependence, achieved by holding inter-mineral partitioning of Fe<sub>2</sub>O<sub>3</sub> constant. We estimated model output uncertainty by propagating uncertainties in the mineral-melt partition coefficients through the model calculation. Model error (1 $\sigma$ ) on Fe<sub>2</sub>O<sub>3</sub>(8) is approximately 0.15 wt% and on Na<sub>2</sub>O(8) is approximately 0.05 wt%

For  $T_p = 1400$  °C and range of  $F = 12$ –20%, we found that a source Fe<sub>2</sub>O<sub>3</sub> concentration of  $0.48 \pm 0.03$  wt% gave the best fit to the MORB data (Fig. 11), which corresponds to a bulk  $D_{Fe_2O_3} = 0.368 \pm 0.057$  and a source Fe<sup>3+</sup>/ΣFe ratio of  $0.053 \pm 0.003$ . To model the effect of varying  $T_p$ , we also performed calculations at  $T_p = 1320$  °C and  $T_p = 1440$  °C, approximately spanning the range of  $T_p$  suggested by Dalton et al. (2014). Because Eq. 2 has a temperature dependence, we can see the effect of the  $T$  dependence of  $D_{Fe_2O_3}^{spl/melt}$  by changing the input temperature of the model (for  $T_p = 1320$  °C bulk  $D_{Fe_2O_3} = 0.387 \pm 0.057$  and for  $T_p = 1440$  °C bulk  $D_{Fe_2O_3} = 0.358 \pm 0.057$ ) and shifting the range of  $F$  upward for higher  $T_p$  and downward for lower  $T_p$ . Dashed curves in Fig. 11 show that the  $T$  dependence of  $D_{Fe_2O_3}^{spl/melt}$  alone captures 41% of the MORB data.

Temperature may have an even larger effect if pyroxene/melt partition coefficients are also sensitive to temperature. Although we do not have sufficient experimental data to test for the effect of temperature on pyroxene/melt partitioning, we can estimate the temperature effect through inter-mineral partitioning between spinel and pyroxenes. We calculated the model again allowing  $D_{Fe_2O_3}^{opx/melt}$  and  $D_{Fe_2O_3}^{cpx/melt}$  to change by fixing the values of  $D_{Fe_2O_3}^{cpx/spi}$  and  $D_{Fe_2O_3}^{opx/cpx}$ . For the same range of potential temperatures and melt fractions, consideration of the pyroxene partition coefficients' temperature dependence causes the model curves to extend to both higher and lower Fe<sub>2</sub>O<sub>3</sub>(8) at a given value of Na<sub>2</sub>O(8) such that the model curves bound 83% of the MORB glasses and capture the entire MORB data array within error when bulk mantle Fe<sub>2</sub>O<sub>3</sub> =  $0.48 \pm 0.03$  wt% (Fig. 11). When pyroxene-melt partition coefficients are allowed to change in this way bulk  $D_{Fe_2O_3}$  for  $T_p = 1400$  remains =  $0.368 \pm 0.057$ , but bulk  $D_{Fe_2O_3}$  changes more strongly with temperature (for  $T_p = 1320$  °C bulk  $D_{Fe_2O_3} = 0.457 \pm 0.057$  and for  $T_p = 1440$  °C bulk  $D_{Fe_2O_3} = 0.314 \pm 0.057$ ). That these model curves span the MORB data suggests that changes in the bulk partition coefficient with  $T_p$  are plausible drivers of MORB Fe<sub>2</sub>O<sub>3</sub>-Na<sub>2</sub>O systematics, and that the ferric iron content of the mantle may be higher than previously thought.

The best-fit source Fe<sub>2</sub>O<sub>3</sub> concentration of  $0.48 \pm 0.03$  wt% is considerably greater than past estimates. Based on correlations between MgO and Fe<sub>2</sub>O<sub>3</sub> in reconstructed whole rock compositions of continental xenoliths, Canil et al. (1994) estimated that Primitive Upper Mantle has 0.3 wt.% Fe<sub>2</sub>O<sub>3</sub> (although we note that this estimate would increase slightly if Canil et al. (1994) had allowed for scant ferric iron in olivine, consistent with Mallmann and O'Neill (2009)). O'Neill et al. (2018) estimated a MORB source with Fe<sub>2</sub>O<sub>3</sub> =  $0.21 \pm 0.06$  wt% from their measurements of Fe<sup>3+</sup>/ΣFe ratios of MORB glasses and using partition coefficients from Mallmann and O'Neill (2009). Shorttle et al. (2015) used Fe<sup>3+</sup>/ΣFe ratios of glasses from Reykjanes Ridge and the Mallmann and O'Neill (2009) partition coefficients to

estimate a MORB source with  $\text{Fe}_2\text{O}_3 = 0.2\text{--}0.45$  wt%, which just overlaps our estimate at the high end. If our model results accurately reflect  $\text{Fe}_2\text{O}_3$  concentrations in the MORB source, then it requires the convecting upper mantle to be significantly more oxidized than peridotites in the continental lithosphere after a similar amount of melt extraction. This difference is great enough that we consider potential flaws in our analysis that may explain the disparity.

Our method of estimating true olivine-pyroxene  $K_D^{\text{Fe-Mg}}$  may be leading to an overestimation of  $\text{Fe}_2\text{O}_3$  concentrations in the pyroxenes. Instead of estimating true  $K_D^{\text{Fe-Mg}}$  as described above, if we set true  $K_D^{\text{Fe-Mg}}$  equal to  $K_D^{\text{Fe-Mg}*}$  of experiment PC216 performed in graphite, then we can test the conservative assumption that the pyroxenes in those experiments have zero  $\text{Fe}_2\text{O}_3$ . When we recalculate pyroxene  $\text{Fe}_2\text{O}_3$  concentrations in this way, the new partition coefficients are  $D_{\text{Fe}_2\text{O}_3}^{\text{opx/melt}} = 0.57 \pm 0.06$  and  $D_{\text{Fe}_2\text{O}_3}^{\text{cpx/melt}} = 0.67 \pm 0.11$ , and the best fit to the MORB array is for source  $\text{Fe}_2\text{O}_3 = 0.45 \pm 0.03$  wt%. The pyroxene  $\text{Fe}_2\text{O}_3$  concentrations in our experiments cannot be lower than this, and resulting partition coefficients still require considerably more MORB-source  $\text{Fe}_2\text{O}_3$  than estimates of other workers.

We may be predicting too great a MORB-source  $\text{Fe}_2\text{O}_3$  concentration if  $\text{Fe}_2\text{O}_3$  in the MORB glasses has been overestimated. Berry et al. (2018) present an alternative method for interpreting Mössbauer spectra of silicate glasses that leads to a XANES calibration that is incompatible with the XANES calibration used by Cottrell et al. (2009), Cottrell and Kelley (2011), and Zhang et al. (2018), which we used to determine  $\text{Fe}^{3+}/\Sigma\text{Fe}$  ratios in the glasses presented here. Although all these studies agree that MORB glasses record a  $f_{\text{O}_2}$  near QFM (Cottrell and Kelley 2011; O'Neill et al. 2018; Zhang et al. 2018), they disagree about what the  $\text{Fe}^{3+}/\Sigma\text{Fe}$  ratio of basalt is as a function of  $f_{\text{O}_2}$ . If the XANES calibration of Cottrell et al. (2009) modified by Zhang et al. (2018) leads to overestimates of  $\text{Fe}_2\text{O}_3$  in silicate glasses, as suggested by Berry et al. (2018), then the ferric iron content in our experimental melts is lower and ferric iron is more compatible in spinel and pyroxene than we report here. At first blush, this would seem to lead to an even higher estimate for mantle ferric iron contents; however, the  $\text{Fe}^{3+}/\Sigma\text{Fe}$  ratios in the MORB glasses would also be overestimated ( $0.14 \pm 0.01$  from Zhang et al. (2018) vs  $0.10 \pm 0.02$  from Berry et al. (2018) such that our model would still overestimate  $\text{Fe}_2\text{O}_3$  of the MORB source. To explore this further, we applied the correction factor supplied by Berry et al. (2018) to our experiments from this study and from the 0.1 MPa study of Davis and Cottrell (2018). The systematic effects of composition and temperature we have described no longer hold, and there is no longer any systematic relationship that explains the variations in  $D_{\text{Fe}_2\text{O}_3}^{\text{spl/melt}}$  from Davis and Cottrell (2018), Sorbadere et al. (2018), Mallmann and O'Neill

(2009), and this study (see Supplementary Figure S8). The modeling we describe above would no longer be valid (see Supplement). Ultimately, interpretation of partitioning in our experiments requires that we choose which method of interpreting the glass Mössbauer spectra is correct, and we choose to follow the Zhang et al. (2018) calibration for the reasons given within Zhang et al. (2018), Cottrell et al. (2021), Borisov et al. (2018), and as further described in the Supplementary text.

Our study may incorrectly ascribe the differences in spinel/melt partitioning between experiments in this study and those from Davis and Cottrell (2018) to temperature when they might instead be a compositional effect. Although the experiments of Mallmann and O'Neill (2009) do not support this interpretation, and our 0.1 MPa experiments demonstrate the temperature effect isolated from changes in spinel composition, future experiments are needed to confirm our results.

### Implications of and supporting evidence for a more oxidized MORB-source mantle

Now let us consider the implications if our modeled MORB source with  $0.48 \pm 0.03$  wt%  $\text{Fe}_2\text{O}_3$  is correct (corresponding to mantle  $\text{Fe}^{3+}/\Sigma\text{Fe}$  ratio =  $0.053 \pm 0.003$ ). It requires that the MORB-source mantle be considerably more oxidized than similarly fertile sub-continental peridotites (Canil et al. 1994). There is already some evidence for this in the xenolith record. Ballhaus (1993) showed that spinel xenoliths from oceanic island basalts (OIB), representing the oceanic lithosphere, are 1–2 log units more oxidized than continental xenoliths with similar spinel Cr# and recording similar temperatures. Cratonic lithospheric mantle in particular has been isolated from mantle convection since its formation, but has been altered since emplacement by transiting melts and fluids (e.g., Menzies et al. 1987). Cratonic lithospheric mantle may have begun just as oxidized as we envision for the modern MORB source and was later reduced by metasomatic fluids. Luth and Stachel (2014) describe just such a scenario and suggest that light rare earth element signatures of cratonic peridotites require concentrations of reducing metasomatic agents sufficient to reset the  $f_{\text{O}_2}$  of the cratonic lithospheric mantle.

A MORB-source more oxidized than implied by continental xenoliths also would bring measured  $f_{\text{O}_2}$  of MORB and model estimates of mantle  $f_{\text{O}_2}$  into agreement. Several different methods of modeling  $f_{\text{O}_2}$  in the mantle find that for a bulk mantle  $\text{Fe}^{3+}/\Sigma\text{Fe}$  ratio of 0.03 (Canil et al. 1994) the shallow mantle should record  $f_{\text{O}_2}$  of about QFM-1, which is in agreement with the continental xenolith record (e.g., Frost and McCammon 2008) but about one log unit more reduced than recorded by average MORB (Cottrell and Kelley 2011; O'Neill et al. 2018; Zhang et al. 2018). Jennings and Holland

(2015) and Stolper et al. (2020) used a THERMOCALC-based model, and Stolper et al. (2020) also used pMELTS, to calculate phase equilibria for a peridotite bulk composition with fixed  $\text{Fe}^{3+}/\Sigma\text{Fe}$  ratio = 0.03 at upper mantle pressures and temperatures. Jennings and Holland (2015) allowed melting to occur and Stolper et al. (2020) suppressed melt formation, but both found that  $f_{\text{O}_2}$  is lower in the spinel peridotite stability field than in the shallowest part of the garnet peridotite stability field. Each predict that spinel-field  $f_{\text{O}_2}$  is in the range QFM-2 to QFM-1. The implications of Jennings and Holland (2015) and Stolper et al. (2020) is that mantle with continental lithosphere-like  $\text{Fe}_2\text{O}_3$  concentrations are more reduced at the depths of MORB generation than QFM, which is the  $f_{\text{O}_2}$  of the MORB source inferred from MORB themselves (Fig. 1; Cottrell and Kelley 2011; O'Neill et al. 2018). It is possible that the process of melt generation itself could lead to oxidation of peridotite as  $\text{Fe}_2\text{O}_3$  is redistributed among the residual phases and the melt. In both a mass balance model and in pMELTS, Gaetani (2016) found that batch melting of peridotite along an adiabatic ascent path leads to oxidation of the residue and melt system by potentially more than a log unit  $f_{\text{O}_2}$ . However, Gaetani's model does not allow for changes to the subsolidus modal mineralogy with temperature, only with pressure. The model does not include temperature effects such as decreasing spinel mode with increasing temperature (Canil and O'Neill 1996) that might counteract the decrease in  $f_{\text{O}_2}$  his model predicts with isobaric heating. The thermodynamic model of Jennings and Holland (2015), which does allow for T-driven variations in mode shows much less variation in  $f_{\text{O}_2}$  along the spinel peridotite solidus than is predicted by Gaetani (2016). The model of Jennings and Holland (2015), which is also a batch melting model, also predicts slight oxidation along an adiabatic ascent path above the solidus, but only predicts 0.2–0.4 log units oxidation. Future models that can incorporate new data about  $\text{Fe}_2\text{O}_3$  partitioning may help to resolve questions of how  $f_{\text{O}_2}$  evolves as melts are extracted beneath ridges.

A more oxidized MORB source has further implications for phase equilibria deeper in the upper mantle. The model of Stagno et al. (2013) predicts that for mantle with  $\text{Fe}^{3+}/\Sigma\text{Fe}$  ratio of 0.03 and bulk  $C = 30$  ppm (which can oxidize 1% of the total Fe in the mantle residue), redox melting will begin at about 150 km depth. A mantle  $\text{Fe}^{3+}/\Sigma\text{Fe}$  ratio between 0.05 and 0.06 would initiate redox melting at depths between 200 and 230 km. This is nearly identical to the range 200–250 km suggested by Dasgupta et al. (2013) that would be consistent with the depth of peak conductivity in the upper mantle (Lizarralde et al. 1995). A more oxidized MORB source than can be predicted from continental xenoliths, therefore, ties together  $f_{\text{O}_2}$  estimates for MORB with thermodynamic models and geophysical evidence for deep onset of melting.

## Conclusions

We performed multiple-saturation experiments at 1.5 GPa, 1350–1400 °C and  $f_{\text{O}_2}$  from ~QFM-3 to QFM+3 using Pt-Fe alloy capsules graphite capsules. We also performed experiments at 0.1 MPa producing spinel–melt pairs at 1300 and 1400 °C. We measured  $\text{Fe}^{3+}/\Sigma\text{Fe}$  ratios in glasses and spinels and we estimate  $\text{Fe}_2\text{O}_3$  of opx and cpx from Mg-Fe exchange between olivine and pyroxenes. We used resulting mineral/melt partition coefficients for  $\text{Fe}_2\text{O}_3$  to model  $\text{Fe}_2\text{O}_3$  and  $\text{Na}_2\text{O}$  concentrations of mantle partial melts. Varying  $T_p$  from 1320 to 1440 °C allows the model to capture ~40% of the variation in MORB  $\text{Fe}_2\text{O}_3(8)\text{-Na}_2\text{O}(8)$  systematics from the temperature dependence of  $D_{\text{Fe}_2\text{O}_3}^{\text{spl/melt}}$  alone. When we allow pyroxene/melt partitioning of  $\text{Fe}_2\text{O}_3$  to vary with temperature through intermineral partitioning between pyroxenes and spinel, the whole MORB data set can be fit within error for the same range of  $T_p$  and source bulk  $\text{Fe}_2\text{O}_3 = 0.48 \pm 0.03$  wt%, corresponding to mantle  $\text{Fe}^{3+}/\Sigma\text{Fe}$  ratio =  $0.053 \pm 0.003$ .

This best-fit source concentration is considerably greater than the widely cited previous estimate of 0.3 wt% from the continental xenolith study of Canil et al. (1994). If our model is correct, then the convecting mantle is more oxidized than the continental lithosphere.

A MORB source at 1 GPa with  $f_{\text{O}_2}$  near QFM (Cottrell and Kelley 2011; O'Neill et al. 2018; Zhang et al. 2018) is more oxidized than continental xenoliths at 1 GPa, which record QFM-1. Therefore, either the process of melting leads to significant oxidation or the MORB-source is more oxidized than the continental lithospheric mantle at the same depth. Our  $\text{Fe}_2\text{O}_3$  partitioning experiments and melting model provide support for the latter. A more oxidized MORB source may also allow for carbon-driven redox melting at depths of high conductivity in the upper mantle between 200 and 250 km (Dasgupta et al. 2013).

**Supplementary Information** The online version contains supplementary material available at <https://doi.org/10.1007/s00410-021-01823-3>.

**Acknowledgements** This manuscript was improved by thoughtful reviews from MR Guild and O Shorttle and from two anonymous reviewers on an earlier version. FD acknowledges support from a Peter Buck Fellowship at the National Museum of Natural History and EC is grateful for a Smithsonian Competitive Grants Program for Science award. We are grateful for assistance from Tony Lanzirrotti, Matt Newville, Tim Gooding, Tim Rose, Suzanne Birner, Marion Le Voyer, Megan Holycross, and Janine Andrys. GeoSoilEnviroCARS is supported by the National Science Foundation—Earth Sciences (EAR-1634415) and Department of Energy- GeoSciences (DE-FG02-94ER14466). Use of the Advanced Photon Source was supported by the DOE Office of Science by Argonne National Laboratory under Contract No. DE-AC02-06CH11357.

**Open Access** This article is licensed under a Creative Commons Attribution 4.0 International License, which permits use, sharing, adaptation, distribution and reproduction in any medium or format, as long as you give appropriate credit to the original author(s) and the source, provide a link to the Creative Commons licence, and indicate if changes were made. The images or other third party material in this article are included in the article's Creative Commons licence, unless indicated otherwise in a credit line to the material. If material is not included in the article's Creative Commons licence and your intended use is not permitted by statutory regulation or exceeds the permitted use, you will need to obtain permission directly from the copyright holder. To view a copy of this licence, visit <http://creativecommons.org/licenses/by/4.0/>.

## References

- Asimow PD (2021) The petrological consequences of the estimated oxidation state of primitive MORB glass. *AGU Geophys Monogr.* <https://doi.org/10.1002/9781119473206.ch7>
- Asimow PD, Ghiorso MS (1998) Algorithmic modifications extending MELTS to calculate subsolidus phase relations. *Am Mineral* 83:1127–1132
- Ballhaus C (1993) Redox states of lithospheric and asthenospheric upper mantle. *Contrib Mineral Petrol* 114:331–348
- Berry AJ, Stewart GA, O'Neill HSC et al (2018) A re-assessment of the oxidation state of iron in MORB glasses. *Earth Planet Sci Lett* 483:114–123
- Bézos A, Humler E (2005) The  $\text{Fe}^{3+}/\Sigma\text{Fe}$  ratios of MORB glasses and their implications for mantle melting. *Geochim Cosmochim Acta* 69:711–725
- Birner SK, Cottrell E, Warren JM et al (2018) Peridotites and basalts reveal broad congruence between two independent records of mantle f O<sub>2</sub> despite local redox heterogeneity. *Earth Planet Sci Lett* 494:172–189
- Blatter DL, Sisson TW, Hankins WB (2013) Crystallization of oxidized, moderately hydrous arc basalt at mid-to lower-crustal pressures: implications for andesite genesis. *Contrib Mineral Petrol* 166:861–886
- Blundy JD, Brodholt JP, Wood BJ (1991) Carbon–fluid equilibria and the oxidation state of the upper mantle. *Nature* 349:321–324
- Blundy J, Falloon T, Wood B, Dalton J (1995) Sodium partitioning between clinopyroxene and silicate melts. *J Geophys Res Solid Earth* 100:15501–15515
- Borisov A, Behrens H, Holtz F (2018) Ferric/ferrous ratio in silicate melts: a new model for 1 atm data with special emphasis on the effects of melt composition. *Contrib Mineral Petrol* 173:98
- Bryndzia LT, Wood BJ (1990) Oxygen thermobarometry of abyssal spinel peridotites: the redox state and C–O–H volatile composition of the Earth's sub-oceanic upper mantle. *Am J Sci* 290:1093–1116
- Canil D, O'Neill HSC (1996) Distribution of ferric iron in some upper-mantle assemblages. *J Petrol* 37:609–635
- Canil D, O'Neill HSC, Pearson D et al (1994) Ferric iron in peridotites and mantle oxidation states. *Earth Planet Sci Lett* 123:205–220
- Christie DM, Carmichael IS, Langmuir CH (1986) Oxidation states of mid-ocean ridge basalt glasses. *Earth Planet Sci Lett* 79:397–411
- Cline C II, Faul U, David E et al (2018) Redox-influenced seismic properties of upper-mantle olivine. *Nature* 555:355
- Cottrell E, Kelley KA (2011) The oxidation state of Fe in MORB glasses and the oxygen fugacity of the upper mantle. *Earth Planet Sci Lett* 305:270–282
- Cottrell E, Kelley KA, Lanzirotti A, Fischer RA (2009) High-precision determination of iron oxidation state in silicate glasses using XANES. *Chem Geol* 268:167–179
- Cottrell E, Lanzirotti A, Mysen B et al (2018) A Mössbauer-based XANES calibration for hydrous basalt glasses reveals radiation-induced oxidation of Fe. *Am Mineral J Earth Planet Mater* 103:489–501
- Cottrell E, Birner S, Brounce M et al (2021) Oxygen fugacity across tectonic settings. *AGU Geophys Monogr.* <https://doi.org/10.1002/9781119473206.ch3>
- Dalton CA, Langmuir CH, Gale A (2014) Geophysical and geochemical evidence for deep temperature variations beneath mid-ocean ridges. *Science* 344:80–83
- Dasgupta R, Mallik A, Tsuno K et al (2013) Carbon-dioxide-rich silicate melt in the Earth's upper mantle. *Nature* 493:211–215
- Davis FA, Cottrell E (2018) Experimental investigation of basalt and peridotite oxybarometers: implications for spinel thermodynamic models and Fe<sup>3+</sup> compatibility during generation of upper mantle melts. *Am Mineral J Earth Planet Mater* 103:1056–1067
- Davis FA, Cottrell E, Birner SK et al (2017) Revisiting the electron microprobe method of spinel-olivine-orthopyroxene oxybarometry applied to spinel peridotites. *Am Mineral* 102:421–435
- Dyar MD, McGuire AV, Ziegler RD (1989) Redox equilibria and crystal chemistry of coexisting minerals from spinel lherzolite mantle xenoliths. *Am Mineral* 74:969–980
- Dyar MD, McGuire AV, Harrell MD (1992) Crystal chemistry of iron in two styles of metasomatism in the upper mantle. *Geochim Cosmochim Acta* 56:2579–2586
- Eugster H (1957) Heterogeneous reactions involving oxidation and reduction at high pressures and temperatures. *J Chem Phys* 26:1760–1761
- Ford C (1978) Platinum-iron alloy sample containers for melting experiments on iron-bearing rocks, minerals, and related systems. *Mineral Mag* 42:271–275
- Fram MS, Longhi J (1992) Phase equilibria of dikes associated with Proterozoic anorthosite complexes. *Am Mineral* 77:605–616
- Frost BR (1991) Introduction to oxygen fugacity and its petrologic importance. *Rev Mineral Geochem* 25:1–9
- Frost DJ, McCammon CA (2008) The redox state of Earth's mantle. *Annu Rev Earth Planet Sci* 36:389–420
- Gaetani G (2016) The behavior of  $\text{Fe}^{3+}/\Sigma\text{Fe}$  during partial melting of Spinel Lherzolite. *Geochim Cosmochim Acta* 185:64–77
- Ghiorso MS, Kress VC (2004) An equation of state for silicate melts. II. Calibration of volumetric properties at 105 Pa. *Am J Sci* 304:679–751
- Ghiorso MS, Sack RO (1995) Chemical mass transfer in magmatic processes IV. A revised and internally consistent thermodynamic model for the interpolation and extrapolation of liquid–solid equilibria in magmatic systems at elevated temperatures and pressures. *Contrib Mineral Petrol* 119:197–212
- Ghiorso MS, Hirschmann MM, Reiners PW, Kress VC (2002) The pMELTS: A revision of MELTS for improved calculation of phase relations and major element partitioning related to partial melting of the mantle to 3 GPa. *Geochem Geophys Geosystems* 3:1–35
- Grove T (1981) Use of FePt alloys to eliminate the iron loss problem in 1 atmosphere gas mixing experiments: Theoretical and practical considerations. *Contrib Mineral Petrol* 78:298–304
- Hauri EH, Cottrell E, Kelley KA et al (2019) Carbon in the convecting mantle. In: Orcutt BN, Daniel I, Dasgupta R (eds) *Deep carbon: past to present*. Cambridge University Press, Deep Carbon, pp 237–275
- Herzberg C, Asimow PD (2008) Petrology of some oceanic island basalts: PRIMELT2. XLS software for primary magma calculation. *Geochem Geophys Geosystems* 9:

- Holloway JR, Pan V, Gudmundsson G (1992) High-pressure fluid-absent melting experiments in the presence of graphite: oxygen fugacity, ferric/ferrous ratio and dissolved CO<sub>2</sub>. *Eur J Mineral* 4:105–114
- Holzheid A, Palme H, Chakraborty S (1997) The activities of NiO, CoO and FeO in silicate melts. *Chem Geol* 139:21–38
- Ionov D, Wood B (1992) The oxidation state of subcontinental mantle: oxygen thermobarometry of mantle xenoliths from central Asia. *Contrib Mineral Petrol* 111:179–193
- Jennings ES, Holland TJ (2015) A simple thermodynamic model for melting of peridotite in the system NCFMASOCr. *J Petrol* 56(5):869–892
- Kessel R, Beckett JR, Stolper EM (2001) Thermodynamic properties of the Pt-Fe system. *Am Mineral* 86:1003–1014
- Klein EM, Langmuir CH (1987) Global correlations of ocean ridge basalt chemistry with axial depth and crustal thickness. *J Geophys Res Solid Earth* 92:8089–8115
- Kress VC, Carmichael IS (1991) The compressibility of silicate liquids containing Fe<sub>2</sub>O<sub>3</sub> and the effect of composition, temperature, oxygen fugacity and pressure on their redox states. *Contrib Mineral Petrol* 108:82–92
- Lizarralde D, Chave A, Hirth G, Schultz A (1995) Northeastern Pacific mantle conductivity profile from long-period magnetotelluric sounding using Hawaii-to-California submarine cable data. *J Geophys Res Solid Earth* 100:17837–17854
- Luth RW, Canil D (1993) Ferric iron in mantle-derived pyroxenes and a new oxybarometer for the mantle. *Contrib Mineral Petrol* 113:236–248
- Luth RW, Stachel T (2014) The buffering capacity of lithospheric mantle: implications for diamond formation. *Contrib Mineral Petrol* 168:1083
- Mallmann G, O'Neill HSC (2009) The crystal/melt partitioning of V during mantle melting as a function of oxygen fugacity compared with some other elements (Al, P, Ca, Sc, Ti, Cr, Fe, Ga, Y, Zr and Nb). *J Petrol* 50:1765–1794
- Mattioli GS, Wood BJ (1988) Magnetite activities across the MgAl<sub>2</sub>O<sub>4</sub>-Fe<sub>3</sub>O<sub>4</sub> spinel join, with application to thermobarometric estimates of upper mantle oxygen fugacity. *Contrib Mineral Petrol* 98:148–162
- McCanta MC, Dyar MD, Rutherford MJ, Delaney JS (2004) Iron partitioning between basaltic melts and clinopyroxene as a function of oxygen fugacity. *Am Mineral* 89:1685–1693
- McGuire AV, Dyar MD, Nielson JE (1991) Metasomatic oxidation of upper mantle peridotite. *Contrib Mineral Petrol* 109:252–264
- Médard E, McCammon CA, Barr JA, Grove TL (2008) Oxygen fugacity, temperature reproducibility, and H<sub>2</sub>O contents of nominally anhydrous piston-cylinder experiments using graphite capsules. *Am Mineral* 93:1838–1844
- Menzies MA, Rogers N, Tindle AG, Hawkesworth CJ (1987) Metasomatic and enrichment processes in lithospheric peridotites, an effect of asthenosphere-lithosphere interaction. In: Menzies MA, Hawkesworth CJ (eds) *Mantle Metasomatism*. Academic Press, London, UK, pp 313–361
- O'Neill HSC, Eggins SM (2002) The effect of melt composition on trace element partitioning: an experimental investigation of the activity coefficients of FeO, NiO, CoO, MoO<sub>2</sub> and MoO<sub>3</sub> in silicate melts. *Chem Geol* 186:151–181
- O'Neill HSC, Berry AJ, McCammon CC et al (2006) An experimental determination of the effect of pressure on the Fe<sup>3+</sup>/ΣFe ratio of an anhydrous silicate melt to 3.0 GPa. *Am Mineral* 91:404–412
- O'Neill HSC, Berry AJ, Mallmann G (2018) The oxidation state of iron in Mid-Ocean Ridge Basaltic (MORB) glasses: implications for their petrogenesis and oxygen fugacities. *Earth Planet Sci Lett* 504:152–162
- Robie RA, Hemingway BS (1995) Thermodynamic properties of minerals and related substances at 298.15 K and 1 bar (10<sup>5</sup> pascals) pressure and at higher temperatures. USGS Bulletin 2131. <https://doi.org/10.3133/b2131>
- Robinson J, Wood B, Blundy J (1998) The beginning of melting of fertile and depleted peridotite at 1.5 GPa. *Earth Planet Sci Lett* 155:97–111
- Rudra A, Hirschmann MM (2019) Experimental determination of ferric iron partitioning between pyroxene and melt during partial melting of the Earth's upper mantle. Abstract V23B-02 Presented at 2019 Fall Meet AGU San Franc CA 9–13 Dec
- Shorttle O, Moussallam Y, Hartley ME et al (2015) Fe-XANES analyses of Reykjanes Ridge basalts: implications for oceanic crust's role in the solid Earth oxygen cycle. *Earth Planet Sci Lett* 427:272–285
- Sorbadere F, Laurenz V, Frost DJ et al (2018) The behaviour of ferric iron during partial melting of peridotite. *Geochim Cosmochim Acta* 239:235–254
- Stagno V, Frost DJ (2010) Carbon speciation in the asthenosphere: experimental measurements of the redox conditions at which carbonate-bearing melts coexist with graphite or diamond in peridotite assemblages. *Earth Planet Sci Lett* 300:72–84
- Stagno V, Ojwang DO, McCammon CA, Frost DJ (2013) The oxidation state of the mantle and the extraction of carbon from Earth's interior. *Nature* 493:84–88
- Stolper EM, Shorttle O, Antoshechkina PM, Asimow PD (2020) The effects of solid–solid phase equilibria on the oxygen fugacity of the upper mantle. *Am Mineral*. <https://doi.org/10.2138/am-2020-7162>
- von Seckendorff V, O'Neill HSC (1993) An experimental study of Fe-Mg partitioning between olivine and orthopyroxene at 1173, 1273 and 1423 K and 1.6 GPa. *Contrib Mineral Petrol* 113:196–207
- Toplis M (2005) The thermodynamics of iron and magnesium partitioning between olivine and liquid: criteria for assessing and predicting equilibrium in natural and experimental systems. *Contrib Mineral Petrol* 149:22–39
- Wood BJ, Virgo D (1989) Upper mantle oxidation state: Ferric iron contents of Iherzolite spinels by 57Fe Mössbauer spectroscopy and resultant oxygen fugacities. *Geochim Cosmochim Acta* 53:1277–1291
- Woodland A, Kornprobst J, Tabit A (2006) Ferric iron in orogenic Iherzolite massifs and controls of oxygen fugacity in the upper mantle. *Lithos* 89:222–241
- Workman RK, Hart SR (2005) Major and trace element composition of the depleted MORB mantle (DMM). *Earth Planet Sci Lett* 231:53–72
- Zhang H, Hirschmann M, Cottrell E, Withers A (2017) Effect of pressure on Fe<sup>3+</sup>/ΣFe ratio in a mafic magma and consequences for magma ocean redox gradients. *Geochim Cosmochim Acta* 204:83–103
- Zhang HL, Cottrell E, Solheid PA et al (2018) Determination of Fe<sup>3+</sup>/ΣFe of XANES basaltic glass standards by Mössbauer spectroscopy and its application to the oxidation state of iron in MORB. *Chem Geol* 479:166–175

**Publisher's Note** Springer Nature remains neutral with regard to jurisdictional claims in published maps and institutional affiliations.